

Elastic extended images and velocity-sensitive objective functions using multiple reflections and transmissions

Matteo Ravasi,¹ Ivan Vasconcelos,² Andrew Curtis¹ and Giovanni Meles¹

¹School of GeoSciences, The University of Edinburgh, Grant Institute, James Hutton Road, Edinburgh EH9 3FE, United Kingdom.

E-mail: M.Ravasi@sms.ed.ac.uk

²Schlumberger Gould Research, High Cross, Madingley Road, Cambridge CB3 0EL, United Kingdom

Accepted 2015 April 16. Received 2015 April 16; in original form 2014 November 3

SUMMARY

One interpretation of a seismic image is the instantaneous scattered wave response of a colocated pseudo-source and pseudo-receiver at each point in the subsurface model. If there is no model perturbation at a point then there will be no instantaneous scattered wave so nothing will be imaged; if something is imaged then there must be a perturbation at that location. By extension, so-called extended images (EIs) represent the full spatio-temporal response between *offset* subsurface pseudo-sources and pseudo-receivers which can be used to constrain elastic properties *around* each image point. However, one-sided illumination of the subsurface (from the Earth's surface), errors in the initial velocity model estimate, and the use of a linearized, single-scattering assumption (as is usual in seismic imaging) cause errors in EI gathers such as missing events, incorrect amplitudes, and spurious energy. By creating elastic (P-to-P and P-to-S) EIs in a synthetic example of subsalt imaging, we demonstrate the advantages of incorporating multiply scattered waves correctly by non-linear imaging, and of including transmitted waves by using two-sided receiver arrays, and discuss how the recently developed autofocussing methods could provide us with the various required subsurface wavefields. Pre- and post-imaging f - k filtering procedures are introduced to further improve the quality of the EIs by (explicitly or implicitly) limiting the directions of waves arriving at the subsurface pseudo-source and receiver survey line. These filters suppress strong linear events that arise from the erroneous interaction of near-horizontally propagating waves which are not naturally accounted for due to the lack of sources and receivers on either side of the imaging target. Finally, we analyse the sensitivity of elastic P-to-P EIs to errors in the migration velocity models and show that events in the EI are shifted in opposite directions when constructed using reflection or transmission data. In other words, velocity errors are mapped into the EIs differently in the case of one-sided from two-sided illumination. This leads to the potential for new methods of migration velocity analysis when surface and borehole seismic data are jointly acquired.

Key words: Interferometry; Controlled source seismology; Wave propagation.

INTRODUCTION

The theory and practice of seismic processing rely on the analysis of recorded seismic data sorted into different domains. Examples include common-shot, common-receiver, common-midpoint or common-offset (Yilmaz 2001). The structure and physical properties of the medium excited during the seismic experiment cannot be inferred directly from a visual inspection of the recorded data in any domain. Nevertheless, important processing procedures such as noise suppression (Canales 1984; Hampson 1987; Jones & Levy 1987), multiple attenuation (Verschuur 1991; Foster & Mosher 1992), velocity analysis (Taner & Koehler 1969) and

amplitude-versus-offset analysis (AVO, Ostrander 1982; Rutherford & Williams 1989; Castagna & Backus 1993) are generally carried out by assuming certain kinematic behaviours of the recorded data in one or more of these domains. After decades of seismic processing experience we understand how different methods allow us to use some of the information best captured within the gathers in each of these domains.

The recent introduction of so-called extended image (EI) gathers allows recorded seismic data to be transformed into approximate time- and space-varying responses between sources and receivers located within the subsurface, without having to have such equipment actually installed there (Vasconcelos *et al.* 2009, 2010;

Halliday & Curtis 2010; Sava & Vasconcelos 2010). These EIs can be used as an alternative to time-lag, space-lag or reflection-angle common image gathers (CIGs) for local velocity analysis around selected image points (Symes 2008; Yang & Sava 2011a,b, 2012; Fleury 2012; Fleury & Perrone 2012), but since they represent source to receiver responses that may be located close to targets of interest they may also be useful for reservoir characterization (Thomson 2012; Vasconcelos & Rickett 2013). To denote that subsurface sources and receivers are virtual rather than real, we call them pseudo-sources and pseudo-receivers henceforth.

Detailed analyses on the form of these gathers, carried out using a geometrical approach (Yang & Sava 2010), asymptotic analysis (Thomson 2012) or stationary-phase analysis (Meles & Curtis 2013; L  er *et al.* 2014) show that the retrieval of the full scattered wavefield response from a pseudo-source to a pseudo-receiver in the subsurface is not always successful. The imprint of finite acquisition geometries (e.g. only one-sided seismic illumination from above) and knowledge of only a smoothed estimate of the propagation velocity model (so that multiples cannot easily be predicted *a priori*, for example) cause errors in the migration process that is used to construct EI gathers. Including multiples and transmitted arrivals in the migration process is thus fundamental if we aim to construct complete and correct EIs, as multiples add some of the missing wave vectors in upward directions, reducing associated errors.

Herein we create and analyse EIs using the source–receiver interferometry (SRI) formulation of Curtis & Halliday (2010), Halliday & Curtis (2010) and Poliannikov (2011) recently adapted to acoustic reverse-time migration by Vasconcelos (2013) and elastic reverse-time migration by Ravasi & Curtis (2013a) and Ravasi *et al.* (2014). We construct elastic (P-to-P and P-to-S) EIs using a complex geological model [a modified version of the Pluto 1.5 model (Stoughton *et al.* 2001)], and analyse the advantage of migrating multiples and transmitted waves together with primary reflections, comparing one-sided linear EIs with one-sided non-linear EIs and those from two-sided imaging. Imaging with multiples is becoming relevant for practical imaging problems because recently developed autofocussing methods offer the possibility to construct Green’s functions from subsurface receivers without actually having to have receivers there (Broggini *et al.* 2012; Wapenaar *et al.* 2012, 2013; da Costa *et al.* 2014a,b,c, Wapenaar & Slob 2014). Two-sided illumination can be achieved by jointly acquiring surface and borehole data or, alternatively, the transmission data may also be estimated by autofocussing. We then introduce two f - k filtering approaches to further improve the quality of the EI gathers: the first is a pre-imaging filter that selects the directions of both incoming and emerging waves used to construct the EI (Vasconcelos *et al.* 2008), whereas the second acts directly on the EI (a post-imaging filter) and can attenuate emerging waves whose dips are outside of a particular range of interest. This analysis shows that while the former more accurately removes unwanted events with possibly different dips in the source and receiver wavefields, the latter approach also performs well and is significantly less costly to apply. Finally, we study the sensitivity of the EIs to errors in the migration velocity models: while it is known that velocity errors in turn cause errors in the EIs, we demonstrate a different sensitivity of transmitted and reflected waves to such errors. We then conjecture that if data are jointly acquired at the Earth’s surface and somewhere inside the medium such as in a borehole, using both transmissions and reflections in objective functions for migration velocity analysis or image-domain waveform inversion could provide more robust velocity estimates than existing methods.

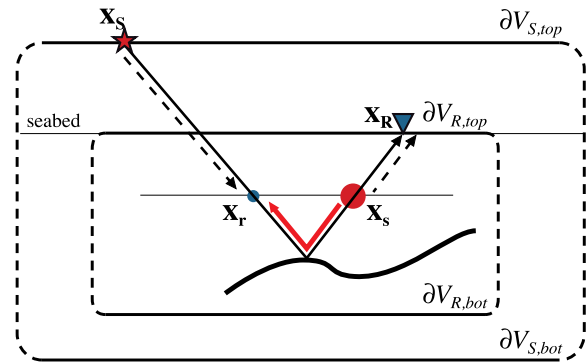


Figure 1. Illustration of the physical meaning of an extended image (EI): a scattered field (red arrow) from a pseudo-source at \mathbf{x}_s (red circle) to a pseudo-receiver at \mathbf{x}_r (blue circle) inside the subsurface. The EI is obtained by means of source–receiver interferometry (SRI) using the recorded data from physical sources \mathbf{x}_S (red star) along the boundary $\partial V_S = \partial V_{S,top} \cup \partial V_{S,bot}$ to physical receivers \mathbf{x}_R (blue triangle) along the boundary $\partial V_R = \partial V_{R,top} \cup \partial V_{R,bot}$ (solid ray), the receiver-side propagators from the pseudo-source \mathbf{x}_s to physical receivers \mathbf{x}_R (right-hand dashed ray), and the source-side propagators from physical sources \mathbf{x}_S to the pseudo-receiver \mathbf{x}_r (left-hand dashed ray). We assume that top and bottom arrays are sufficiently extensive that contributions from arrays on the left or right (dashed) boundary segments are negligible.

ELASTIC EIs BY SRI IMAGING

Our goal is to adapt the elastic source–receiver imaging framework presented in Ravasi & Curtis (2013a) and Ravasi *et al.* (2014) to construct elastic EIs. Similarly to the definition of a usual seismic image, an EI can be seen as a scattered field associated with pseudo-sources and pseudo-receivers inside the subsurface as displayed by the red arrow in Fig. 1 (Vasconcelos *et al.* 2009; Halliday & Curtis 2010; Sava & Vasconcelos 2010; Vasconcelos *et al.* 2010). Different combinations of pseudo-source types and pseudo-receiver quantities can be used to construct EIs. For example, the scattered wavefield from an external volume force pseudo-source at \mathbf{x}_s to a particle-velocity pseudo-receiver at \mathbf{x}_r at a given time t will be denoted $EI_{ji}(\mathbf{x}_r, \mathbf{x}_s, t) = G_{(i,j)}^{S(v,f)}(\mathbf{x}_r, \mathbf{x}_s, t)$, and the scattered wavefield from a potential (P - or S -wave) pseudo-source at \mathbf{x}_s to a potential (P or S wave) pseudo-receiver at \mathbf{x}_r at a given time t will be denoted $EI_{MN}(\mathbf{x}_r, \mathbf{x}_s, t) = G_{(N,M)}^{S(\phi,\phi)}(\mathbf{x}_r, \mathbf{x}_s, t)$. In our notation G denotes a Green’s function, the two superscripts between brackets define the observed quantity and the source type respectively. The components of the observed quantity and the source quantity are further specified by the subscripts: specifically, subscripts i and j in $G_{(i,j)}^{S(v,f)}$ identify the i th component of the particle velocity receivers (denoted v in the superscript) and the j th component of the external volume force sources (f), while subscript capital letters N and M in $G_{(N,M)}^{S(\phi,\phi)}$ refer to potentials (ϕ) and can be chosen to be P or S to identify P - or S -wave potential virtual sources and receivers in the subsurface, respectively. Note that a further superscript S is added to emphasize that the EI represents the scattered wavefield component of the Green’s function (the component of the wavefield that cannot be simulated using the reference model) rather than the complete Green’s function (which we denote with no additional superscript) or the Green’s function through the reference model (which we denote with a superscript 0).

EIs can be constructed via SRI (Curtis & Halliday 2010; Halliday & Curtis 2010; Vasconcelos 2013; Ravasi & Curtis 2013a) using two-way representation theorems for elastic scattered waves (Wapenaar & Fokkema 2006; van Manen *et al.* 2006; Curtis & Halliday

2010) as shown in Fig. 1. Consider an ocean-bottom acquisition scenario with pressure (P wave) sources and multicomponent receivers placed along a flat, horizontal seabed. An elastic imaging condition which preserves both the time and space correlation lags for potential-to-potential responses can be written (Ravasi & Curtis 2013b)

$$\begin{aligned}
 EI_{MN}^{nl}(\mathbf{x}_r, \mathbf{x}_s, t) &= G_{(N,M)}^{S(\phi,\phi)}(\mathbf{x}_r, \mathbf{x}_s, t) + G_{(N,M)}^{S(\phi,\phi)}(\mathbf{x}_r, \mathbf{x}_s, -t) \\
 &\approx \int \left(\int_{\partial V_S} \frac{2}{\rho(\mathbf{x}_S) c_P(\mathbf{x}_S)} \Phi_M^S(\mathbf{x}_s, \mathbf{x}_S) G_{(N,P)}^{0(\phi,\phi)*}(\mathbf{x}_r, \mathbf{x}_S) d\mathbf{x}_S \right) e^{-j\omega t} d\omega \\
 &\quad + \int \left(\int_{\partial V_S} \frac{2}{\rho(\mathbf{x}_S) c_P(\mathbf{x}_S)} \Phi_M^S(\mathbf{x}_s, \mathbf{x}_S) G_{(N,P)}^{S(\phi,\phi)*}(\mathbf{x}_r, \mathbf{x}_S) d\mathbf{x}_S \right) e^{-j\omega t} d\omega,
 \end{aligned} \tag{1}$$

where the G and Φ terms represent the frequency domain source- and receiver-side wavefields, respectively; the former is a wavefield modelled directly from the source at \mathbf{x}_S to the pseudo-receiver location \mathbf{x}_r , while the latter is the wavefield that is recorded by the receivers at \mathbf{x}_R and back-extrapolated to the pseudo-source location \mathbf{x}_s , as shown below. As mentioned above, here superscripts 0/S are added to discriminate the reference/scattered fields from the full fields (the latter is written without a superscript 0 or S), ρ is the density and c_P is the P -wave velocity at the boundary of sources ∂V_S (both of which can be moved outside of the integrals if they do not vary around the boundaries), ω is the angular frequency, and * denotes complex conjugation in the frequency domain (or time-reversal in time domain). Receiver-side potential wavefields Φ are back-extrapolated in an elastic fashion using another representation theorem of correlation-type (Ravasi & Curtis 2013a):

$$\begin{aligned}
 \Phi_M^S(\mathbf{x}_s, \mathbf{x}_S) &= \int_{\partial V_R} \left(p^S(\mathbf{x}_R, \mathbf{x}_S) G_{(M,z)}^{0(\phi,f)*}(\mathbf{x}_s, \mathbf{x}_R) \right. \\
 &\quad \left. - v_z^S(\mathbf{x}_R, \mathbf{x}_S) G_{(M,zz)}^{0(\phi,h)*}(\mathbf{x}_s, \mathbf{x}_R) \right) d\mathbf{x}_R \\
 &\quad + \int_{\partial V_R} \left(p(\mathbf{x}_R, \mathbf{x}_S) G_{(M,z)}^{S(\phi,f)*}(\mathbf{x}_s, \mathbf{x}_R) \right. \\
 &\quad \left. - v_z(\mathbf{x}_R, \mathbf{x}_S) G_{(M,zz)}^{S(\phi,h)*}(\mathbf{x}_s, \mathbf{x}_R) \right) d\mathbf{x}_R,
 \end{aligned} \tag{2}$$

and

$$\begin{aligned}
 \Phi_M^S(\mathbf{x}_s, \mathbf{x}_S) &= \int_{\partial V_R} \left(p(\mathbf{x}_R, \mathbf{x}_S) G_{(M,z)}^{(\phi,f)*}(\mathbf{x}_s, \mathbf{x}_R) \right. \\
 &\quad \left. - v_z(\mathbf{x}_R, \mathbf{x}_S) G_{(M,zz)}^{(\phi,h)*}(\mathbf{x}_s, \mathbf{x}_R) \right) d\mathbf{x}_R,
 \end{aligned} \tag{3}$$

where p and v_z are the pressure and vertical particle velocity recordings needed for the extrapolation, and G are the numerically modelled propagators. Superscripts f and h define external volume force sources and external deformation rate sources, respectively, and subscripts z/zz identify the z th/ zz th component of these sources with z being the vertically downgoing depth coordinate. Note that Einstein's summation convention of summing over all values of repeated indices is not applied in equations herein. Finally, an elastic wavefield separation procedure must be applied at each image point to both the source and the receiver wavefields to discriminate P - or S -wave potential fields from the full elastic wavefield. Helmholtz decomposition of the particle velocity vector field can

be used for the homogeneous and isotropic elastic wave equation (Aki & Richards 2002), while a projection of the vector field onto the polarization vector is required for anisotropic media (see, e.g. Yan 2010).

The combination of eqs (1)–(3) give rise to non-linear elastic EIs and we refer to this imaging procedure as non-linear elastic reverse-time migration (NLERTM). In this context, non-linearity refers to the fact that the second integral in eqs (1), (2) and the integral in eq. (3) include combinations of measured scattered fields with other scattered field propagators. Hence these combinations involve quadratic (hence non-linear) contributions of the unknown scattered wavefields, and include all orders of interactions of waves with the scattering components of the medium (for example, all orders of multiple scattering from non-smooth medium perturbations). Calculating these latter terms generally requires that the scattering (non-smooth) part of the medium is known prior to imaging.

When only a (usually smooth) reference model is available as is commonly the case prior to imaging, only reference Green's functions with few if any reflected or diffracted waves may be available. A linearized, approximate EI can then be obtained by simply dropping all of the non-linear terms from the combination of eqs (1), (2) and (3) (Ravasi & Curtis 2013a):

$$\begin{aligned}
 EI_{MN}^l(\mathbf{x}_r, \mathbf{x}_s, t) &= \int \left(\int_{\partial V_S} \frac{2}{\rho(\mathbf{x}_S) c_P(\mathbf{x}_S)} G_{(N,P)}^{0(\phi,\phi)*}(\mathbf{x}_r, \mathbf{x}_S) \right. \\
 &\quad \times \int_{\partial V_R} \left(p^S(\mathbf{x}_R, \mathbf{x}_S) G_{(M,z)}^{0(\phi,f)*}(\mathbf{x}_s, \mathbf{x}_R) \right. \\
 &\quad \left. \left. - v_z^S(\mathbf{x}_R, \mathbf{x}_S) G_{(M,zz)}^{0(\phi,h)*}(\mathbf{x}_s, \mathbf{x}_R) \right) d\mathbf{x}_R d\mathbf{x}_S \right) e^{-j\omega t} d\omega.
 \end{aligned} \tag{4}$$

The latter authors show that eq. (4) is the dynamically correct version of the heuristically derived imaging condition of Yan & Sava (2008), correctly accounting for heterogeneities in velocity and density parameters around the source boundary. We refer to this imaging procedure as elastic reverse-time migration (ERTM). Moreover, as shown in Fig. 1, here we adopt the following convention: one-sided illumination refers to $\partial V_R = \partial V_{R,top}$ and $\partial V_S = \partial V_{S,top}$, while two-sided illumination refers to $\partial V_R = \partial V_{R,top} \cup \partial V_{R,bot}$ and $\partial V_S = \partial V_{S,top}$. Although having also two-sided source illumination $\partial V_S = \partial V_{S,top} \cup \partial V_{S,bot}$ would without doubt provide further information, we do not consider that case here.

Pseudo common-shot and common-receiver gathers (but also similarly common-midpoint and common-offset gathers) can be created based on different choices of pseudo-sources \mathbf{x}_s and pseudo-receivers \mathbf{x}_r . It is important to remember that the field associated with a pseudo-source is obtained by back-propagation of recorded elastic data (i.e. wavefield extrapolation—eqs 2 and 3), while the pseudo-receiver field comes from the direct forward modelling of the source wavefield. While the choice of the type of pseudo-gather we want to reconstruct is irrelevant for pure-mode EIs like $EI_{PP}^l(\mathbf{x}_r, \mathbf{x}_s, t)$ or $EI_{SS}^l(\mathbf{x}_r, \mathbf{x}_s, t)$ because pseudo-sources and pseudo-receivers can simply be swapped by invoking source-receiver reciprocity (Wapenaar & Fokkema 2006), extra care must be taken for converted-mode EIs, especially when constructing linear P -to- S EIs ($EI_{PS}^l(\mathbf{x}_r, \mathbf{x}_s, t)$) using migration velocity models that do not contain any sharp boundaries. This is because S -wave energy needed to construct the EI cannot be generated in the source wavefield from a P -wave source without an accurate knowledge of one

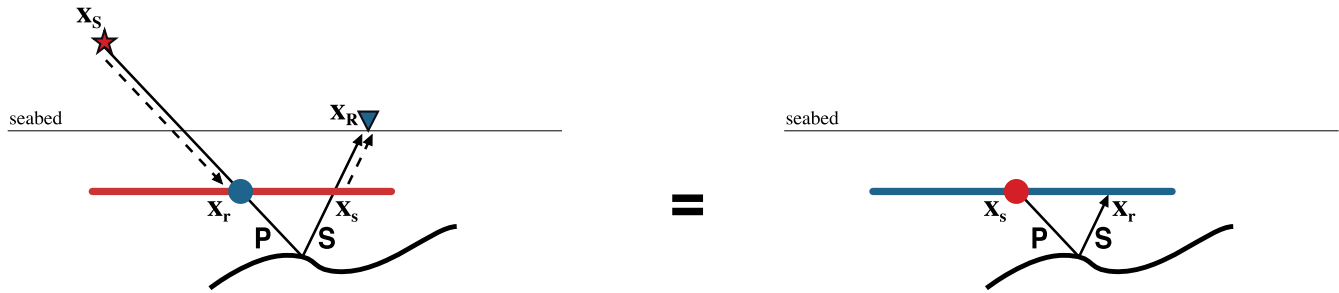


Figure 2. Schematic representation of the construction of the P-to-S pseudo common-shot gather $EI_{PS}(x_r, x_s, t)$. The S-to-P pseudo common-receiver gather from a line of pseudo-sources at x_s (red line) to a pseudo-receiver at x_r (left) is constructed by back-propagating the S -wave energy which is recorded along the receiver array in the physical experiment to position x_r . Using source–receiver reciprocity, the latter also represents the P-to-S pseudo common-shot gather (right) from a pseudo-source at x_s to a line of pseudo-receivers at x_r (blue line).

or more sharp boundaries in the velocity and/or density models. We notice however that a S-to-P pseudo common-receiver gather can be constructed by exploiting the S -wave energy recorded along the receiver array in the physical experiment and back-propagating it in an elastic manner by the first term of eq. (2) through any type of migration model, even one without sharp boundaries. Finally then, we convert this gather into a P-to-S pseudo common-shot gather using source–receiver reciprocity (Fig. 2). Note that, for simplicity, we follow the same procedure to construct P-to-P EIs in the numerical example below, although pseudo common-shot gathers could have been produced directly when imaging using pure-mode waves.

PRE- AND/OR POST-IMAGING F - K FILTERING

Eqs (1) to (4) contain cross-correlations (one term convolved with the conjugate of another) within all integrands, and each integrand has been shown to be equivalent to an instance of correlational seismic interferometry (Curtis 2009; Curtis & Halliday 2010; Halliday & Curtis 2010). In seismic imaging, as well as in interferometry, non-physical energy arises from the cross-correlation of source and receiver wavefields when either the wavefields that are correlated are incomplete, or they are integrated over incomplete boundaries ∂V_R and ∂V_S (Snieder *et al.* 2006; King *et al.* 2011; King & Curtis 2012). This is especially the case in the presence of complex velocity or density models that contain sharp, dipping discontinuities such as salt flanks: in such cases, different orders of waves propagating along the pseudo-receiver line (e.g. near-horizontally propagating waves when using horizontal lines of pseudo-receivers) correlate with each other and generate strong cross-talk events in the EIs.

We can take advantage of the fact that this type of non-physical energy is constructed from, and appears in, different f - k bands from most of the desired physical energy: two different f - k filtering approaches can be used to improve the quality of the retrieved EIs in terms of mitigating non-physical (hence undesired) events. The first procedure steers the directivity of both pseudo-sources and pseudo-receivers. It is based on the observation that by limiting the direction of incoming waves at the pseudo-receiver location and the direction of emerging waves at the pseudo-source location, we also select a range of local dips of reflectors/discontinuities whose effect will be included in the EI (Vasconcelos *et al.* 2008), thus eliminating, for example, the non-physical contributions from steeply dipping reflectors. We design two band-pass filters in the wavenumber domain, H_ϕ and H_G , which respectively select a range of incident and emerging angles and filter out waves that are outside of the defined ranges. Thus we prevent undesired waves (arriving

at the pseudo-source or pseudo-receiver from directions outside of these ranges) from interacting together within the imaging condition in eq. 1, and thus from creating artefacts in the EI (Fig. 3). In practice filters H_ϕ and H_G are applied to the receiver and source wavefield in the frequency–wavenumber domain, and the filtered responses are then transformed back to frequency–space domain via an inverse Fourier transform:

$$\widehat{\Phi}_M(x_s, x_s, \omega) = \int H_\phi(\mathbf{k}_s) \Phi_M(\mathbf{k}_s, x_s, \omega) e^{-j\mathbf{x}_s \mathbf{k}_s} d\mathbf{k}_s \quad (5)$$

and

$$\widehat{G}_{(N,P)}^{(\phi, \phi)}(x_r, x_s, \omega) = \int H_G(\mathbf{k}_r) G_{(N,P)}^{(\phi, \phi)}(\mathbf{k}_r, x_s, \omega) e^{-j\mathbf{x}_r \mathbf{k}_r} d\mathbf{k}_r, \quad (6)$$

where $\widehat{\Phi}$ and \widehat{G} are the filtered receiver and source wavefields, respectively, \mathbf{k}_s is the apparent pseudo-source wavenumber vector (wavenumbers measured from the receiver wavefield at the EI survey line via a spatial Fourier transform) and \mathbf{k}_r is the apparent pseudo-receiver wavenumber vector (wavenumbers measured from the source wavefield at the EI survey line via a spatial Fourier transform).

Alternatively, we can act on the EI directly and shape the directivity of pseudo-receivers. Since spurious events due to waves propagating along the EI survey line tend to occur in a particular sector of the wavenumber spectrum (near the critical angle), that is at least partially non-overlapping with physical events, waves in that sector can be removed by applying a spatial band-pass filter H_{EI} that preserves only dips inside a range of interest in the EI gather (Fig. 3). The filter H_{EI} is applied to the frequency–wavenumber EI,

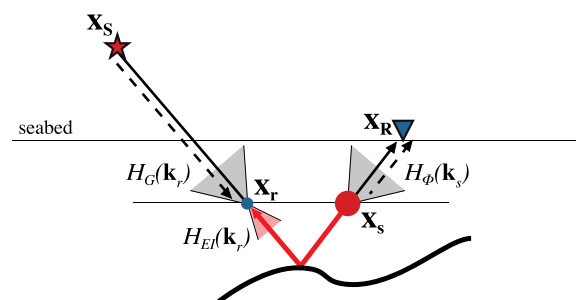


Figure 3. Illustration of the effect that the bandpass filters H_ϕ , H_G and H_{EI} have on the source wavefield, receiver wavefield, and extended image respectively. For each, a range of incident or emerging angles is selected (grey cones for pre-imaging filtering and red cone for post-imaging filtering); waves that are outside of the defined ranges are filtered out in order to prevent non-physical artifacts appearing in the extended image.

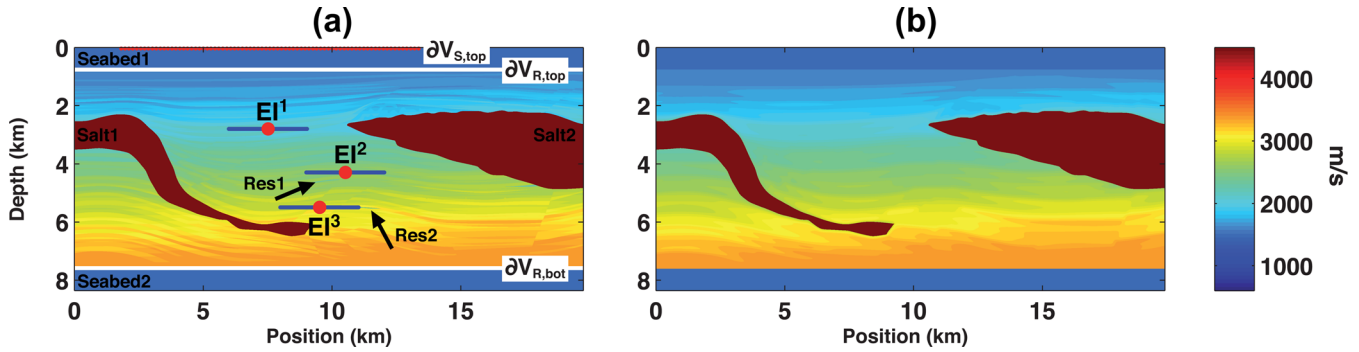


Figure 4. (a) Stratigraphic P -wave velocity model, shot locations (red line at top) and receiver geometry (white lines at top and bottom of the solid medium). Here the EIs pseudo-survey geometries are also displayed: red dots represent the pseudo-sources, blue lines identify the pseudo-receiver arrays. Res1 and Res2 indicate locations of the two reservoirs. (b) Smoothed P -wave velocity model used for linear migration.

and the filtered EI is then transformed back to frequency–space domain via an inverse Fourier transform:

$$\widehat{EI}_{MN}(\mathbf{x}_r, \mathbf{x}_s, \omega) = \int H_{EI}(\mathbf{k}_r) EI_{MN}(\mathbf{k}_r, \mathbf{x}_s, \omega) e^{-j\mathbf{x}_r \cdot \mathbf{k}_r} d\mathbf{k}_r. \quad (7)$$

Eqs (5)–(7) represent multidimensional inverse Fourier transforms that map $\mathbf{k}_s \rightarrow \mathbf{x}_s$ and $\mathbf{k}_r \rightarrow \mathbf{x}_r$. Note that cut-off wavenumbers in the pre-imaging approach are directly linked to cut-off incident and emerging angles, θ_ϕ and θ_G , and can be obtained by:

$$\begin{aligned} k_{s, \text{cut-off}}(\omega) &= \pm \frac{\omega}{\bar{c}_M} \sin(\theta_\phi), \\ k_{r, \text{cut-off}}(\omega) &= \pm \frac{\omega}{\bar{c}_N} \sin(\theta_G), \end{aligned} \quad (8)$$

where $\bar{c}_{M/N}$ is the average (P - or S -wave velocity) along the pseudo-survey line, with M and N referring to the wave type at the pseudo-source and pseudo-receiver, respectively. Similarly, cut-off wavenumbers in the post-imaging approach are obtained by:

$$k_{r, \text{cut-off}}(\omega) = \pm \frac{\omega}{\bar{c}_N} \sin(\theta_{EI}), \quad (9)$$

where θ_{EI} is the cut-off dip in the EI.

EXAMPLE

We present a numerical example where P-to-P and P-to-S EIs are reconstructed at three different subsurface locations using a modified version of the synthetic dataset Pluto 1.5 released by the SMAART JV consortium (Stoughton *et al.* 2001). The seabed is flattened at a depth of $z_{\text{seabed},1} = 760$ m, and a second water layer is added at the bottom of the model ($z_{\text{seabed},2} = 7600$ m) so that we can correctly extrapolate the recorded (pressure and vertical particle velocity) data using eqs (2) and (3) also along the receiver boundary below the imaging target (otherwise additional horizontal particle velocity and shear stress recordings would be required as explained in Ravasi & Curtis (2013a)). The P -wave stratigraphic velocity model is displayed in Fig. 4(a) and the S -wave velocity model is a scaled version of the P -wave velocity with a linearly depth-varying ratio ranging from 0.5 at $z_{\text{seabed},1}$ to 0.7 at $z_{\text{seabed},2}$. The ratio is however kept constant inside the two salt bodies ($V_S/V_P = 0.55$). The density is obtained from the P -wave velocity through Gardner's relationship $\rho = 0.23 V_p^{0.25}$ (Gardner *et al.* 1974). The reference model used for linear imaging (eq. 4) is shown in Fig. 4(b). It is a smooth version of the model in Fig. 4(a) with hard boundaries kept at the fluid–solid interfaces and at the edges of the salt bodies.

A truncated, limited-aperture boundary of 154 monopole P -wave sources at a depth of $z_S = 40$ m with horizontal spacing of $dx_S = 76$ m (red line in Fig. 4a) is used to model the synthetic data together with two boundaries of multicomponent seabed receivers (white lines in Fig. 4a) placed along the upper and lower boundaries of the solid medium across the full extent of the model with horizontal spacing of $dx_R = 7.6$ m. Wavefield modelling is carried out using a Ricker wavelet pulse with 15 Hz peak frequency and a maximum recording time of 10s. Absorbing boundaries are used (to remove the effects of the free-surface), otherwise further dipole P -wave sources would be required to decompose in- and out-going waves at the source boundary ∂D_S (Vasconcelos 2013).

We choose to place our EI *pseudo-surveys* beside features of the model indicated in Fig. 4(a). The first EI is relatively shallow ($z_{EI,1} = 2800$ m), at a depth comparable with the top interface of both salt bodies. Since sources provide a good illumination of the pseudo-survey line, a reasonable EI should be obtained even when only top sources and receivers are used along with conventional imaging. However strong waves propagating sub-horizontally, which bounce multiple times between the two salt bodies and pass through the pseudo-survey line, will create spurious events in the EI. This is the ideal scenario to test the effectiveness of our two f - k filtering approaches. Noting that the model contains two small reservoirs around ($x = 10\,000$ m, $z = 4500$ m) and ($x = 11\,000$ m, $z = 5500$ m), the second and third EIs are placed at $z_{EI,2} = 4300$ m and $z_{EI,3} = 5500$ m, respectively, and they are analysed in the Supporting Information.

In the following, four imaging experiments which are schematically visualized in Fig. 5 (and are similar to those analysed for conventional zero-offset imaging in Ravasi *et al.* 2014) are used to discuss the importance of both multiply reflected and transmitted waves in extended imaging. A similar analysis is performed by Meles & Curtis (2013) and L er *et al.* (2014) in the context of source–receiver interferometry using a stationary-phase approach under the assumption of single-scattering by a diffractor, and L er *et al.* (2014) and Meles & Curtis (2014a,b) also consider multiply-diffracted waves. The examples here go beyond those previous studies in that (1) they represent an imaging experiment where apart from the recorded data (fields from physical sources recorded at physical receivers), all the other fields are computed numerically and are subject to errors due to the approximate reference velocity models used; (2) they are performed in a complex model where the contribution of multiple-scattering both by reflections and diffractions is significant and (3) they go beyond the acoustic approximation and they effectively represent the first examples

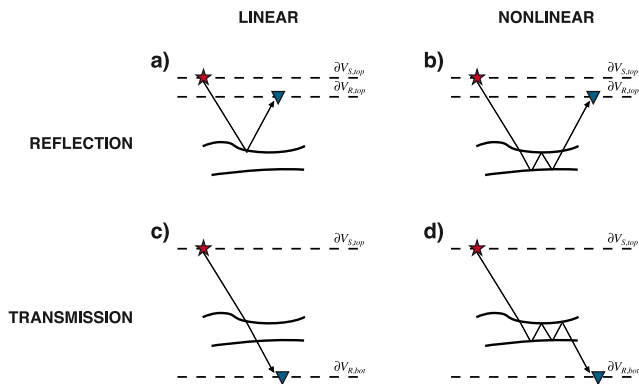


Figure 5. Schematic representation of the four different imaging experiments. (a) Reflection (one-sided receiver illumination from the top) elastic reverse-time migration (ERTM – which is linear). (b) Reflection non-linear elastic reverse-time migration (NLERTM). (c) Transmission (one-sided receiver illumination from the bottom) ERTM. (d) Transmission NLERTM. Black rays identify schematically the type of events accounted for in each of the experiments: one-sided imaging uses reflections only, whereas two-sided imaging uses transmissions to improve the imaging result. Linear imaging only accounts for focusing of the primary reflections and transmissions, while non-linear imaging also uses multiple reflections, and transmissions with multiple reflections correctly.

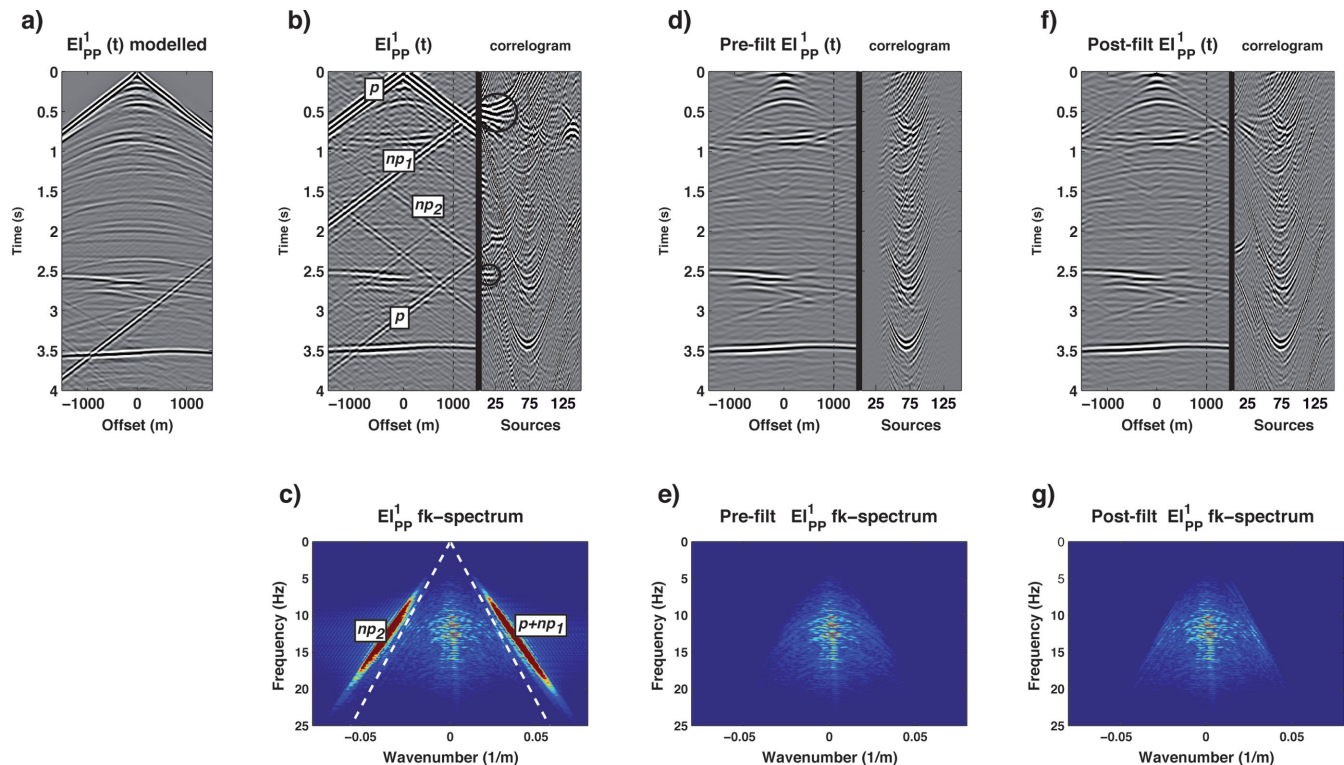


Figure 6. Application of the pre- and post-imaging f - k filters to the linear P-to-P extended image shown in (b) together with its source correlation gather for the pseudo-receiver at 1000 m offset (i.e. integrand in eq. 4 before stacking over sources). The directly modelled EI is shown in (a) for comparison. The f - k amplitude spectrum in (c) shows that physical energy with hyperbolic moveout is present at low wavenumbers and is fairly distinct from physical energy with linear moveout (label p) and spurious energy (labels np_1 and np_2) populating the high wavenumbers of the spectrum. Limiting the incident and emerging angles to lie between $\pm 50^\circ$ suppresses the linear events from the extended image as shown in gather (d), and (e) is its f - k amplitude spectrum. Applying only a post-imaging filter limiting dips to lie in the range of $\pm 50^\circ$ (see white dashed lines in (c)) also produces a reasonable EI as displayed in (f) and (g). Note that the pre-imaging filter has suppressed more energy due to external sources in the source correlation gather (d) than has the post-imaging filter in the source correlation gather (f). Similarly the energy near the critical angle is weaker in the pre-imaging f - k spectrum than in the post-imaging one. Hence, these filters could provide fairly different results for situations where the physical stationary points are due to sources at the edge of the boundary.

of elastic EIs in complex media (linear or non-linear) presented to date.

P-to-P EIs

Recalling that an EI represents (in theory) the response from a pseudo-source to a pseudo-receiver inside the subsurface (Fig. 1), we first model the exact response for the shallow pseudo-survey geometry shown in Fig. 4(a) from a P -wave pseudo-source to a line of P -wave pseudo-receivers (Fig. 6a). Fig. 6(b) shows the causal part of the P-to-P EI obtained by means of reflection ERTM. We observe that dominant events mainly show a linear moveout, which suggests that they are created by the interaction of waves propagating sideways along the pseudo-receiver array. Although some of these linear events are physical (as indicated by the labels p), the others are spurious or non-physical (np) events and strongly interfere with most of the physical waves that show much smaller amplitudes. Events exhibiting different moveouts in the t - x domain are mapped onto different wavenumbers in the f - k domain, and in this case most of the physical energy is mapped to lower wavenumbers than the non-physical (unwanted) energy (Fig. 6c). We first apply the f - k filtering procedure which acts in the pre-imaging domain to select waves with incident and emerging angles limited to lie between $\pm 50^\circ$, constructing the EI from the filtered source and receiver fields obtained from eqs (5) and (6) (Fig. 6d). Spurious

events are successfully suppressed and the physical events in the selected range of angles are now enhanced in the EI (see also the f - k spectrum in Fig. 6e). This filtering approach is very effective but it is also expensive because a multidimensional Fourier transform has to be applied to both the source and receiver wavefields for each shot. We also apply the second f - k filtering approach which acts directly on the EI (i.e. the post-imaging f - k filter) where we remove events with a dip higher than $\pm 50^\circ$ (Figs 6f and g). This example shows that, given proper tuning of the filters H_ϕ , H_G or H_{EI} , both the pre- and post-imaging filtering procedures provide clearer EIs compared to the original (pre-filtered) one. In the following, we apply the post-imaging filter to all PP EIs that are shown.

Fig. 7 compares $EI_{PP}^1(\mathbf{x}_r, \mathbf{x}_s, t)$ obtained from the imaging experiments in Fig. 5. The filtered exact response is shown in Fig. 7(a) with green and magenta arrows used to indicate upgoing and downgoing waves. Starting from the reflection ERTM EI (Fig. 7b), we first notice how upgoing events (green arrows), such as reflections coming from the top of the salt and the seabed (*salt1* and *seabed2* in Fig. 4a), are generally constructed in the causal part, while downgoing events (magenta arrows) are constructed in the anticausal part. This is especially clear when we observe the first 0.5 s, where reflections from thin layers just above and below the EI survey line are constructed. To determine the origin of the events constructed it is useful to analyse the so-called correlation gather (van Manen *et al.* 2005; Mehta *et al.* 2008; L  er *et al.* 2014). The correlation gather is simply the set of integrands that are integrated in the imaging (and interferometric) eqs (1)–(4). The dominant contribution for each source or receiver on the boundary to the summation or integration is represented by energy with zero gradient with respect to the boundary location—so-called stationary points (Snieder 2004). In SRI two correlation gathers can be analysed: the correlation gathers for each receiver pair in the first step (intersource interferometry or, equivalently, wavefield extrapolation as in eqs 2 and 3), and the correlation gather for each source pair in the second step (inter-receiver interferometry or, equivalently, the imaging condition as in eq. 1). In the following we will limit our analysis to the source correlation gather for one pseudo-receiver, namely the pseudo-receiver at 1000 m offset. By looking at the correlation gather at positive times (Fig. 6f), we can see that stationary points of upgoing events are located in the centre of the source array. A similar observation could be drawn by looking at the correlation gather for downgoing waves at negative times: however, although the construction of upgoing events is purely physical as displayed in Fig. 8(a), downgoing events are generated in a non-physical manner (Fig. 8b) as also noticed by Poliannikov (2011). Finally, physical events with linear moveout (Fig. 6b) are stationary with respect to only a few sources on the left side (see black circles in the source correlation gather). The creation of these events is only enabled by the presence of the interpreted (sharp-boundaried) salt bodies in the background models which act as secondary sources (Fig. 8c), and by turning waves (Fig. 8d) in the reference propagators which construct stationary paths that would otherwise have been present only if sources and receivers on the sides of the model were available (red lines in Figs 8c and d).

We now create the EI from NLERTM (Fig. 7d). We also display the purely non-linear contributions (Fig. 7c), obtained by subtracting from Fig. 7(d) the linear term (eq. 4), that is displayed in Fig. 7(b). The non-linear terms are beneficial in a number of ways: first, multiples are successfully used to construct events in the pseudo-gather by means of scattered propagators, which add energy to those events obtained by conventional linear imaging (see, for example, that although most of the energy in the event at 3.5 s arises from linear

interactions in Fig. 7(b), non-linear interactions provide additional energy—Fig. 7(c)—that cannot be discarded if we want to obtain reliable amplitudes in the EIs). Secondly, multiples also provide non-physical contributions that either totally or partially cancel those arising in ERTM. As a result, the energy mapped around zero-offset and zero-time is better focused for NLERTM (close-up in Fig. 7d) than for ERTM (close-up in Fig. 7b); this feature of the non-linear EI is directly linked to the overall improvement in the image resolution of non-linear over conventional linear imaging due to proper use of multiply scattered waves (Vasconcelos 2013; Ravasi & Curtis 2013b; Ravasi *et al.* 2014) and share similarities with super-resolution effects in ultrasound imaging (Simonetti 2006; Lerosey *et al.* 2007; Fink 2008). On the other hand, the increased complexity of non-linear source and receiver wavefields makes the cross-talk more severe and the EI noisier overall, as is also observed in acoustic non-linear imaging by Vasconcelos (2013).

The advantage of also having receivers below the imaging target can be appreciated by inspection of the EIs from transmission ERTM (Fig. 7e), the non-linear part of transmission NLERTM (Fig. 7f) and their sum (namely transmission NLERTM, Fig. 7g). Overall, transmitted data from top sources are mainly responsible for constructing upgoing waves in the anticausal part (as demonstrated explicitly later on) and downgoing waves in the causal part. Moreover the downgoing reflection from the top seabed is reconstructed here for the first time. Interestingly this event as well as the upgoing reflections from the bottom seabed, show incorrect polarity when obtained with ERTM (Fig. 7e), which is however correct in the non-linear contributions present in NLERTM (Fig. 7f). Fleury & Vasconcelos (2012) noticed a similar behaviour in the image domain for acoustic waves, where the conventional image exhibits incorrect polarity for some of the reflectors which is corrected by the addition of non-linear imaging terms.

In our final experiment receivers are simultaneously present above and below the target. Both reflection and transmission responses are thus used to create the EIs as shown in Fig. 7(h). Note the good match between this response and the directly modelled EI in Fig. 7(a). It is also important to observe that causal and anticausal parts become very similar in terms of event construction and amplitudes when two-sided non-linear imaging is performed. Since the final EI should converge to the causal and anticausal Green's function if both top and bottom sources and receivers were used, the degree to which time symmetry in the gather is achieved constitutes a means to assess the quality of the Green's function reconstruction, a criterion that is commonly used in seismic interferometry from ambient noise (see Stehly *et al.* 2006).

P-to-S EIs

Analogously to our study of P-to-P EIs, we now analyse the construction of the converted-wave P-to-S response $EI_{PS}^1(\mathbf{x}_r, \mathbf{x}_s, t)$. The directly modelled pseudo common-shot gather from a P -wave pseudo-source to a line of S -wave pseudo-receivers is displayed in Fig. 9(a). The reconstructed EIs are displayed in the other panels of Fig. 9 (the same f - k filter is applied to each EI as discussed below). In the process of constructing P-to-S responses from elastic data a number of differences with their P-to-P counterparts can be observed.

First, two types of strong linear cross-talk events contaminate the converted-wave EIs (Fig. 10a): one type has similar dip to that of P-to-P EIs and another type has higher dip (see the f - k spectrum in Fig. 10b). Our pre- and post-imaging f - k filters are again used to enhance the physical arrivals as shown in Figs 10(c) and (e).

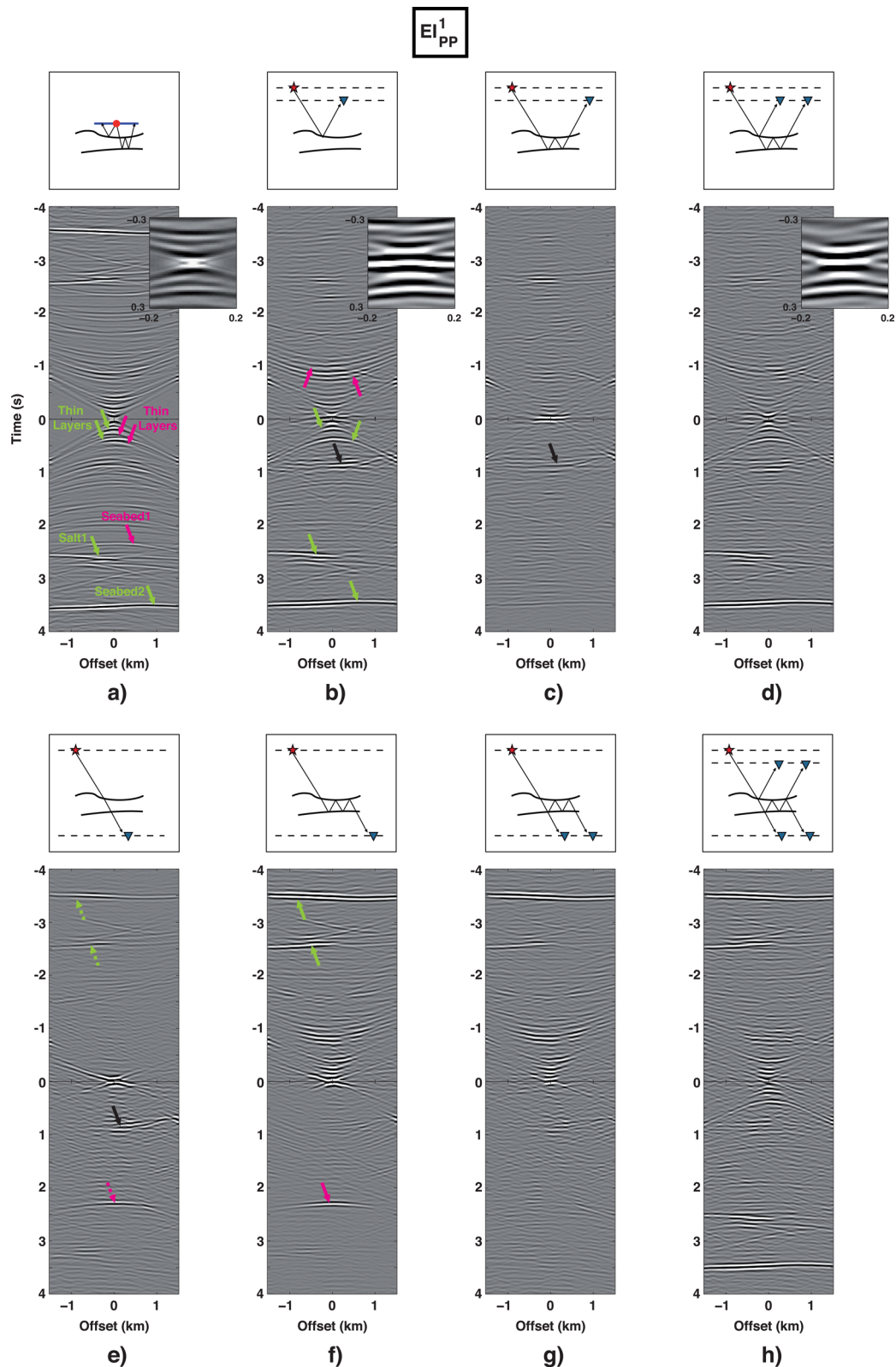


Figure 7. P-to-P extended images obtained (a) via direct modelling and (b–h) from the four imaging experiments depicted in Fig. 5 (and from various summed combinations of their contributions) for the first (shallow) survey line $EI_{PP}^1(x_r, x_s, t)$. The same post-imaging f - k filter has been applied to all panels. Green/magenta solid arrows point at up-/downgoing events (solid arrow: correct amplitude, dashed arrow: incorrect amplitude), and additional black arrows identify non-physical events which are not suppressed by the post-imaging f - k filters but which are suppressed by using non-linear imaging. Close-ups in (a), (b) and (d) show focusing around the zero-time and zero-offset (imaging) point.

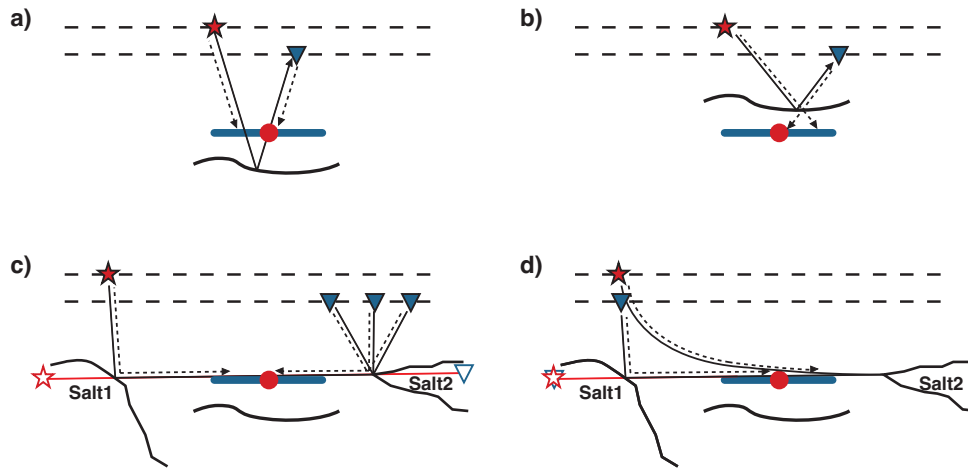


Figure 8. Stationary points of four different types of physical and non-physical events generated by reflection ERTM in Figs 6(b) and 7(b). Solid lines represent the reflection event contained in the recorded data, while dashed lines are used for the propagators that are applied to the data to undo the propagation effect from and to the real sources and receivers towards the pseudo-survey line. (a) Physical construction of an upgoing event and (b) non-physical construction of a downgoing event. Construction of (c) the direct wave and (d) a diffraction from the edge of the salt enabled by the presence of sharp discontinuities and a velocity gradient creating turning waves in the background model. A red line together with an open red star and blue triangle is added to plots (c) and (d) to indicate a boundary source–receiver pair that would be needed to construct the same event in the absence of secondary scattering in the reference propagators.

The filtered EIs are clearer compared to the original (pre-filtered) one (Fig. 10a), and the pre-imaging filter is more effective than the post-imaging filter in attenuating spurious energy while preserving the original amplitude of physical events (refer to Fig. 9a for a comparison with amplitudes of events in the true EI).

Second, the interaction between P - and S -waves in the source and receiver wavefields generates other cross-talk events with a peculiar reverse move-out (see, for example, the event at 1 s in Fig. 9e). These events, although clearly non-physical, cannot be removed easily by an f - k filtering approach since they are mapped to wavenumbers where physical events are also mapped. Once again non-linear imaging provides equivalent non-physical events (Fig. 9g) that cancel those of linear imaging (see Fig. 9f).

Although we have shown that we are able to construct P-to-S EIs that contain some useful information (the reflection from the top of salt1 indicated in Fig. 9a, and from layers just above and below the EI survey line are, for example, reconstructed in Fig. 9h), the overall quality of these pseudo-gathers is poor compared to that of P-to-P gathers. Such a difference between P-to-P and P-to-S EIs can be explained by the fact that stationary contributions needed to construct physical events (and to cancel spurious arrivals) in their pseudo-gathers are distributed differently along the boundaries of sources ∂V_S and receivers ∂V_R for compressional and shear waves. While the acquisition geometry used in this imaging experiment (Fig. 4a) is sufficient to capture most of the physical stationary contributions needed for P-to-P EIs while limiting contributions from non-physical points, many more spurious stationary contributions appear in the construction of P-to-S EIs as discussed further below.

Another factor that could explain the deterioration in quality of the reconstruction at later times in the P-to-S EI (especially in the anticausal panels) is the recording time for each shot; while 10 s is probably sufficient to record most of the primary (and multiple) P -wave reflections and transmissions, some of the later S -wave conversions are left out in the data (see Fig. 4b) and consequently in the corresponding EIs. Given the recording time of 10 s to 12 s per shot in standard marine acquisition, and due to the limits of computing power available, we did not simulate longer records to test this, but it nevertheless seems reasonable. A third possibility

is that marine-type P -wave source geometries provide insufficient illumination of the various shear wavefields that may be produced. For example, with horizontal seabeds at which shear tractions are zero it is impossible to generate horizontal shear energy in the solid seabed using acoustic sources above (or below) the solid model. To generate such energy would require pressure source arrays on either side of the model, or shear sources on the seabed, neither of which were included here in order to make the computational power requirements tractable.

SENSITIVITY OF THE EIs TO VELOCITY ERRORS

An EI contains both focusing information from time-lags and move-out information from space-lags that can be employed together for migration velocity analysis (MVA) as shown for pure-mode waves by Yang & Sava (2011a,b, 2012), Fleury (2012), and Fleury & Perrone (2012) and for converted-waves by Yan & Sava (2010) and Shabelansky *et al.* (2013). In fact, errors in the migration velocity models lead to a departure of the focusing from zero-lag, and to deformation of the moveout in the space-lag. After we have shown that an EI is an approximation to a scattered field in the subsurface, we can move beyond these geometrical arguments and may design new migration velocity analysis objective functions based on the physical meaning of the EI as a Green's function.

To study this, new EIs are generated using incorrect P - and S -wave velocity models formed by adding a +10 per cent error everywhere, apart from inside the salt bodies and the water layers where the correct velocities are maintained. Here we limit the source acquisition boundary to half of its original extension (i.e. $\partial V_S/2$) and sampling (i.e. $dx_S/2$). Fig. 11 displays $EI_{PP}^1(\mathbf{x}_r, \mathbf{x}_s, t)$ for the different imaging experiments: when the EI is obtained by means of reflection ERTM, having incorrect (too fast) migration propagators results in a shift of the events in the gather to later times: for example the event at ~ 2.5 s in Fig. 7b (a reflection from the salt body on the left) moves to ~ 2.7 s (Fig. 11b). This shift can be explained by considering the construction of an up-going reflection event by means of a stationary phase approach (Fig. 12a): this event is

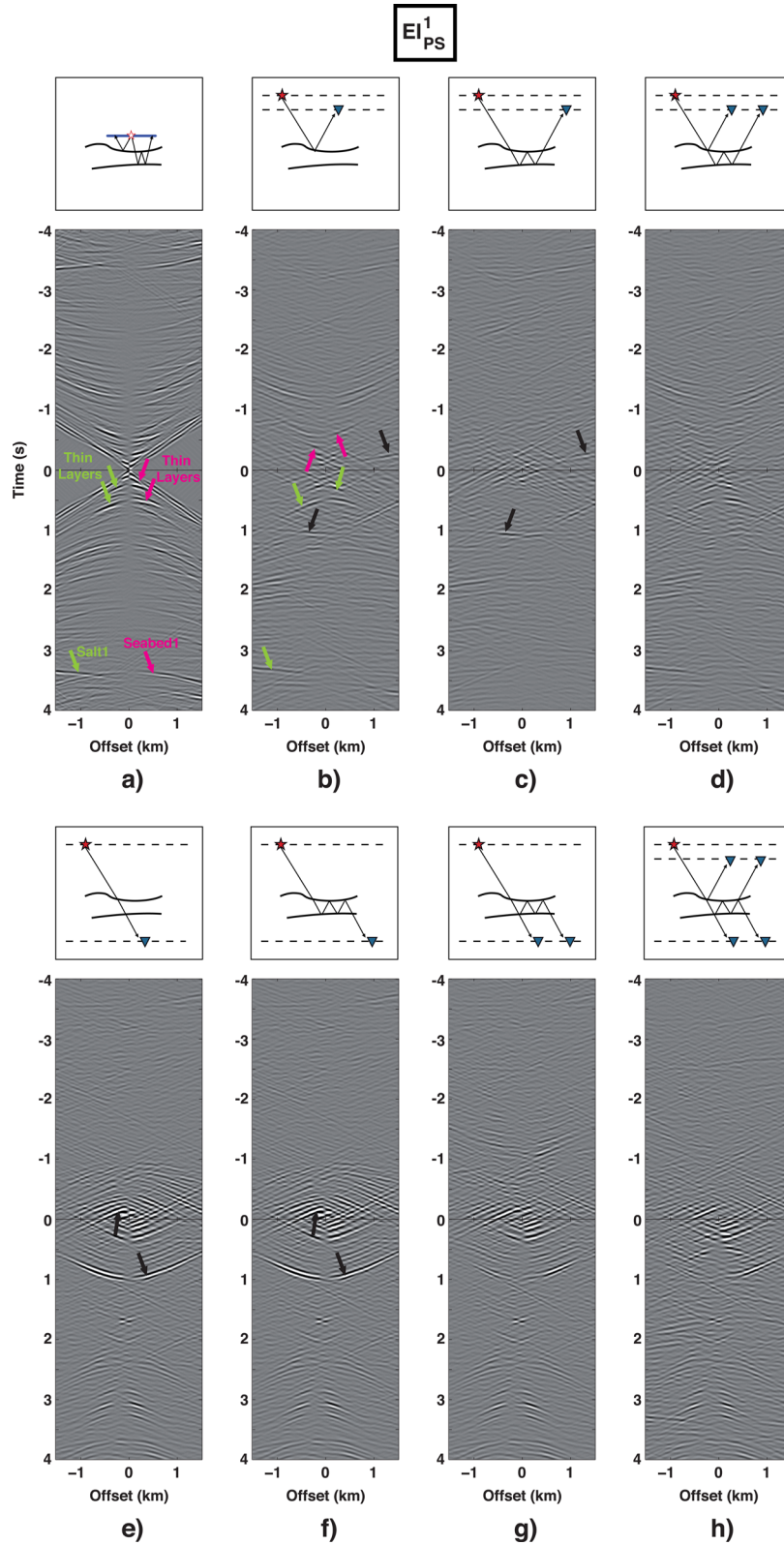


Figure 9. P-to-S extended images obtained (a) via direct modelling and (b–h) from the four imaging experiments depicted in Fig. 5 (and from various summed combinations of their contributions) for the first (shallow) survey line $EI_{PS}^1(x_r, x_s, t)$. Key as in Fig. 7.

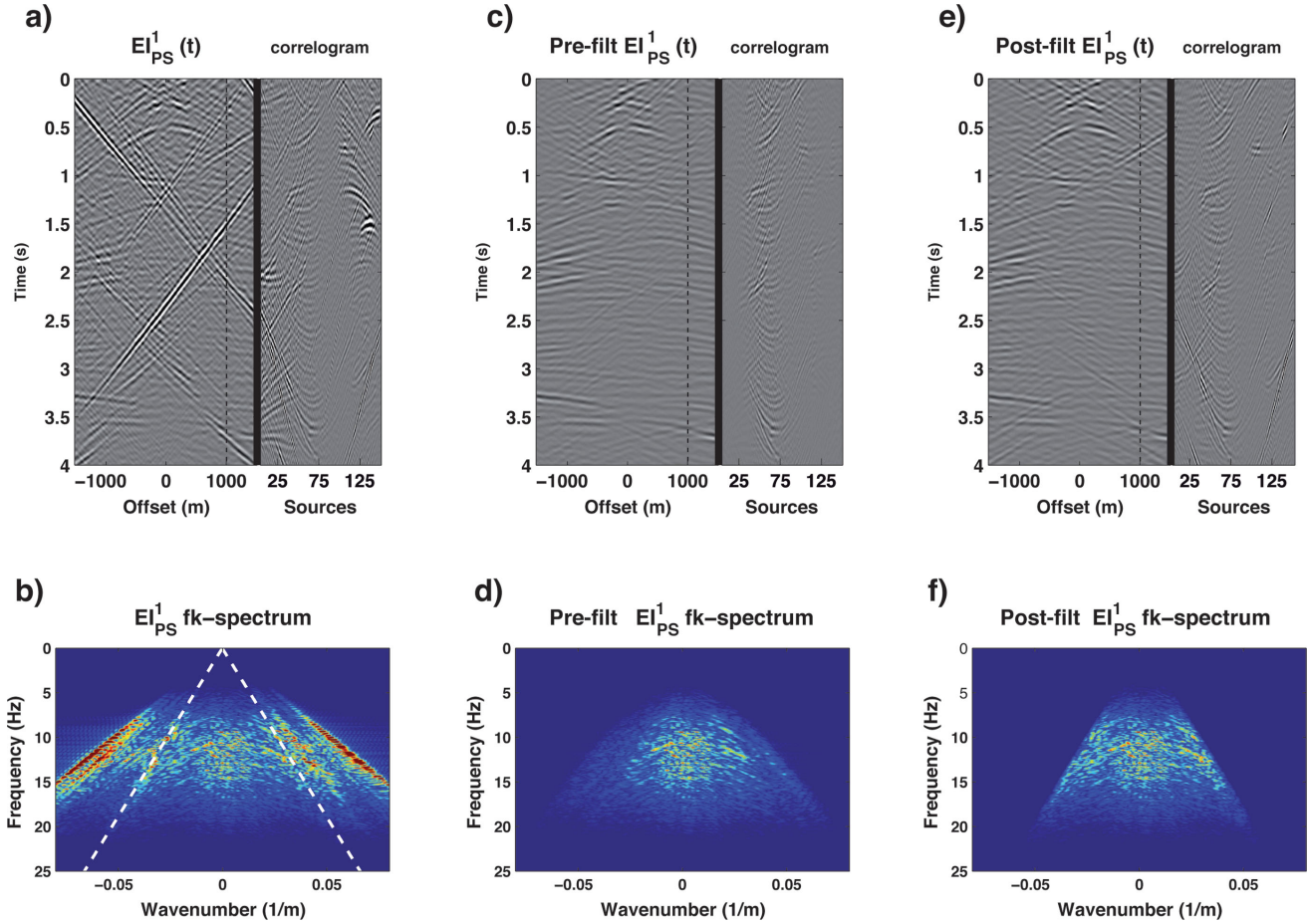


Figure 10. Application of the pre- and post-imaging f - k filters to the P-to-S linear extended image $EI_{PS}^1(\mathbf{x}_r, \mathbf{x}_s, t)$ shown in (a). The f - k amplitude spectrum in (b) is wider compared to that in Fig. 7(b) and the distinction between physical and non-physical energy is less clear. By limiting the incident and emerging angles between $\pm 40^\circ$ in the pre-imaging filtering procedure, the EI is successfully deprived of spurious energy as displayed in (c) [and in its f - k spectrum in (d)]. The post-imaging filter, designed to limit dips to lie in the range of $\pm 40^\circ$ [white dashed lines in (b)], is less successful in removing the artefacts due to the contribution of external sources (e), from which energy can also be seen near the critical angle in the related f - k spectrum. The added value of the pre-imaging filtering approach is that it limits dips in the source wavefield as well as in the receiver wavefield.

created by subtracting from the traveltimes of the fixed, observed reflection in the data ($t_{\mathbf{x}_S \rightarrow \mathbf{x}_R}$) the traveltimes of the propagators from the physical source to the pseudo-receiver ($t_{\mathbf{x}_S \rightarrow \mathbf{x}_r}$) and from the physical receiver to the pseudo-source ($t_{\mathbf{x}_R \rightarrow \mathbf{x}_s}$):

$$t_{\mathbf{x}_s \rightarrow \mathbf{x}_r} = t_{\mathbf{x}_S \rightarrow \mathbf{x}_R} - t_{\mathbf{x}_R \rightarrow \mathbf{x}_s} - t_{\mathbf{x}_S \rightarrow \mathbf{x}_r}. \quad (10)$$

When the propagators are computed in the incorrect (overestimated) velocity models their traveltimes $t_{\mathbf{x}_S \rightarrow \mathbf{x}_r}^{v_{10\%}}$ and $t_{\mathbf{x}_R \rightarrow \mathbf{x}_s}^{v_{10\%}}$ are smaller than the correct ones, so the resulting EI traveltimes is larger than the one from the correct velocity models:

$$t_{\mathbf{x}_s \rightarrow \mathbf{x}_r}^{v_{10\%}} = t_{\mathbf{x}_S \rightarrow \mathbf{x}_R} - t_{\mathbf{x}_R \rightarrow \mathbf{x}_s}^{v_{10\%}} - t_{\mathbf{x}_S \rightarrow \mathbf{x}_r}^{v_{10\%}} > t_{\mathbf{x}_s \rightarrow \mathbf{x}_r}. \quad (11)$$

A similar exercise can be repeated to explain the shift of events in the other panels (Figs 11c–h).

Specifically, when we look at up-going waves constructed from the energy of reflected waves (mainly populating the causal part in Figs 11b and c) and those employing the energy from transmitted waves (mainly populating the anticausal part in Figs 11e and f), we note that they are shifted from their original location in opposite directions with slightly different time-shifts. For example the strong reflection from the bottom seabed is at time 3.5 s in the EI constructed with correct velocity (Fig. 7h), but the same event moves to 3.7 s in the causal part of the EI constructed with incor-

rect velocity (Fig. 11h) and to -3 s in the anticausal part of the same EI (Fig. 11h). We now seek to understand this in more detail, and will show below that it leads to a new velocity discrimination criterion.

Meles & Curtis (2013) and L er *et al.* (2014) analyse the contribution of each individual term in scattered wave SRI using a stationary phase approach. Under the assumption of a localized perturbation (e.g. a single point diffractor) located below the pseudo-survey line, they show that only two terms actually create physical energy contributions in the Green's function reconstructions (equations B1 to B3 in L er *et al.* 2014). Using our notation these terms can be written as:

$$EI_{MN}^{f,f}(\mathbf{x}_r, \mathbf{x}_s, t) = \int \left(\int_{\partial V_{S,top}} \frac{2}{\rho(\mathbf{x}_S) c_P(\mathbf{x}_S)} G_{(N,P)}^{0(\phi,\phi)*}(\mathbf{x}_r, \mathbf{x}_S) \times \int_{\partial V_{R,top}} \left(p^S(\mathbf{x}_R, \mathbf{x}_S) G_{(M,z)}^{0(\phi,f)*}(\mathbf{x}_s, \mathbf{x}_R) - v_z^S(\mathbf{x}_R, \mathbf{x}_S) G_{(M,zz)}^{0(\phi,h)*}(\mathbf{x}_s, \mathbf{x}_R) \right) d\mathbf{x}_R d\mathbf{x}_S \right) e^{-j\omega t} d\omega, \quad (12)$$

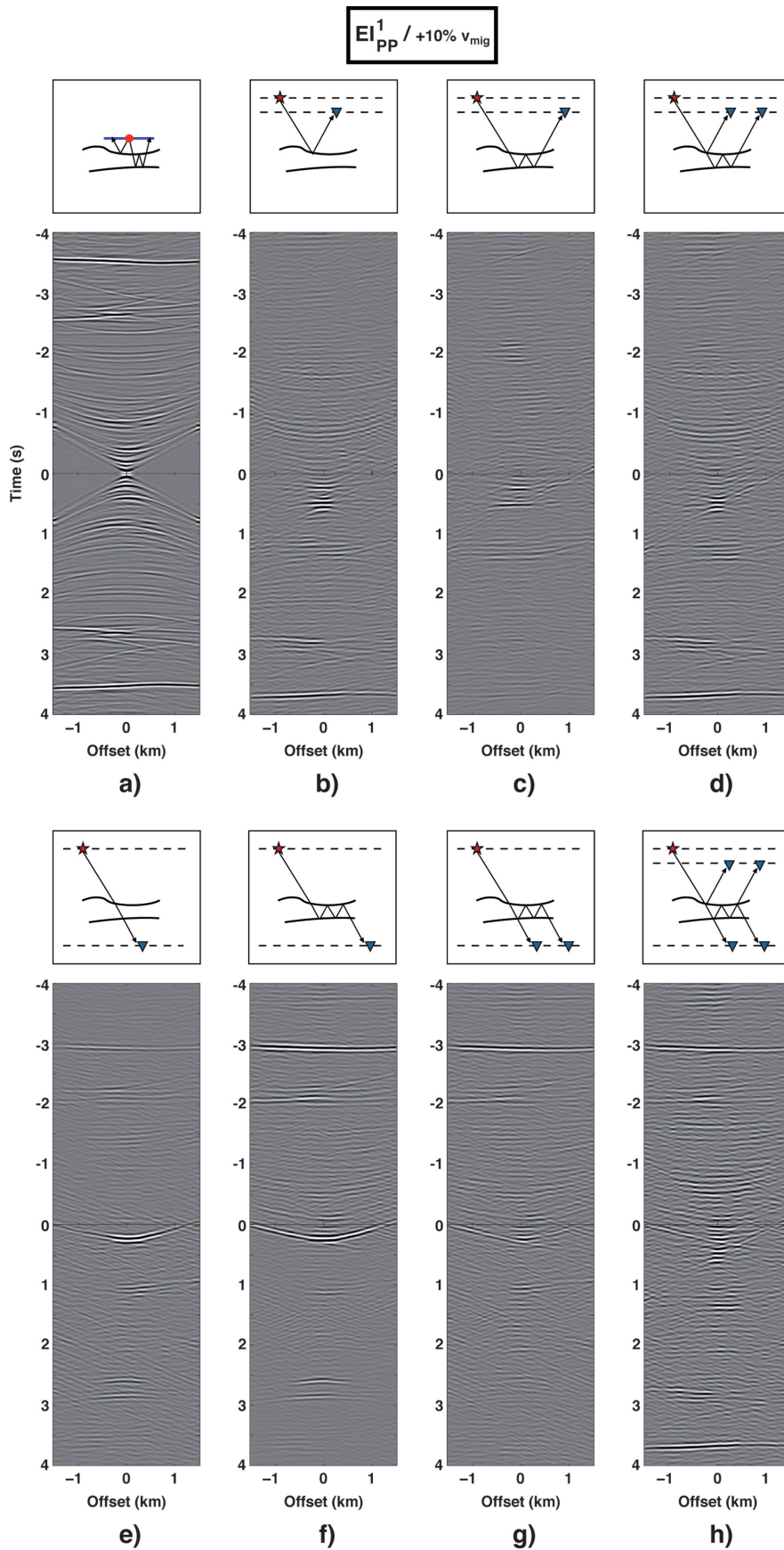


Figure 11. P-to-P extended images obtained (a) via direct modelling with the correct velocity models and (b–h) from the four different experiments depicted in Fig. 5 (and from various summed combinations of their contributions) for the first survey line $EI_{PP}^1(x_r, x_s, t)$, using *P*- and *S*-wave reference and total velocity models with a +10 per cent error in the migration propagators. Events are generally shifted downward in the causal parts and upward in the anticausal parts.

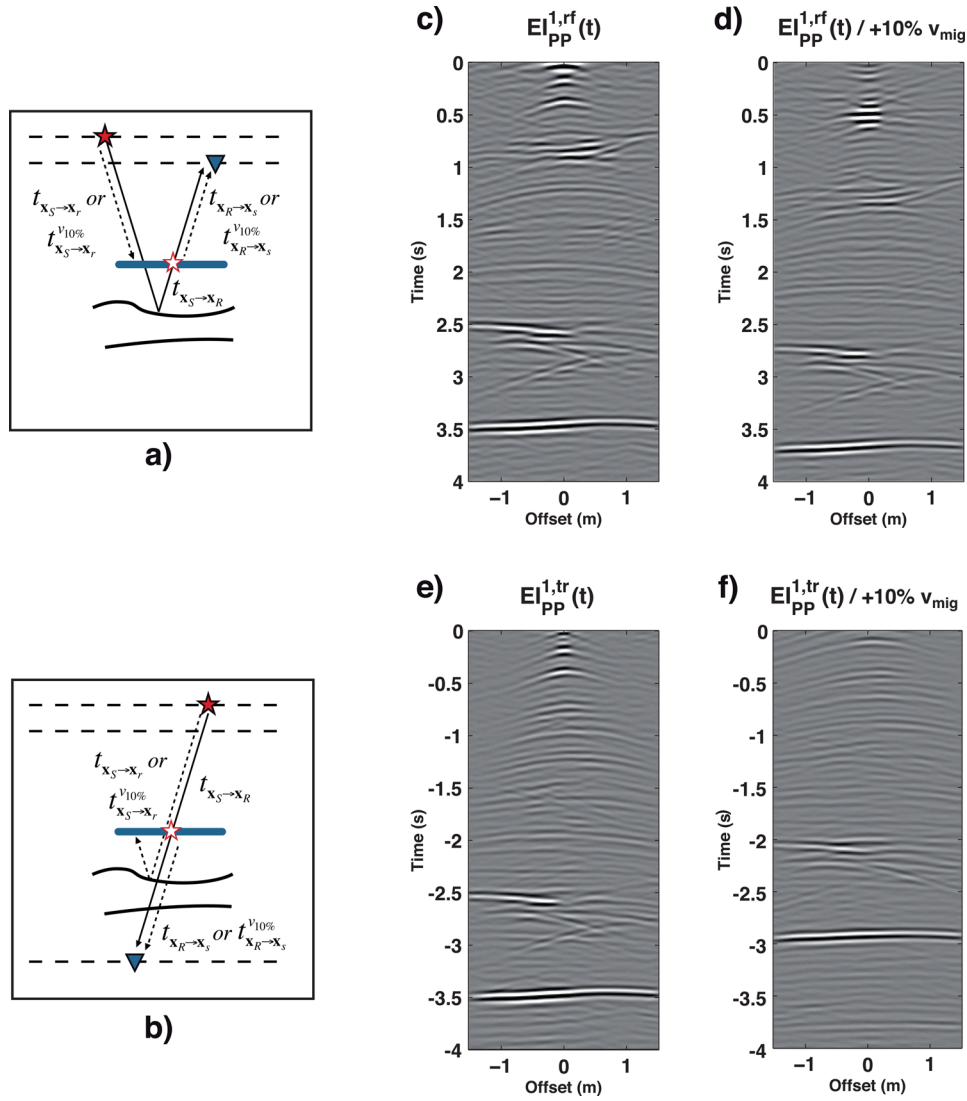


Figure 12. Terms that provide physical contributions to the construction of P-to-P reflections. The causal contribution comes from linear imaging of reflection data [panel (a) and eq. 12], here shown for EI_{PP}^1 with (c) correct velocity models and (d) incorrect velocity models. Non-linear imaging of transmitted data is responsible for the creation of the anticausal contribution for (e) correct velocity models and (f) incorrect velocity models [see panel (b) and eq. 13]. Solid lines in the illustrations represent the data (reflections in top plots and transmissions in lower plots) whereas dashed lines represent the propagators that are applied to the data.

and

$$EI_{MN}^{tr}(\mathbf{x}_r, \mathbf{x}_s, t) = \int \left(\int_{\partial V_{S,top}} \frac{2}{\rho(\mathbf{x}_S) c_P(\mathbf{x}_S)} G_{(N,P)}^{S(\phi,\phi)*}(\mathbf{x}_r, \mathbf{x}_S) \right. \\ \times \int_{\partial V_{R,bot}} \left(p^0(\mathbf{x}_R, \mathbf{x}_S) G_{(M,z)}^{0(\phi,f)*}(\mathbf{x}_s, \mathbf{x}_R) \right. \\ \left. \left. - v_z^0(\mathbf{x}_R, \mathbf{x}_S) G_{(M,zz)}^{0(\phi,h)*}(\mathbf{x}_s, \mathbf{x}_R) \right) d\mathbf{x}_R d\mathbf{x}_S \right) e^{-j\omega t} d\omega. \quad (13)$$

The reflection-related term EI_{MN}^{rf} contributes to the causal Green's function (Fig. 12a) and shows how conventional imaging from above using reflection data and a background model (within the G^0 terms) maps unknown discontinuities in the subsurface. The

transmission-related term EI_{MN}^{tr} constructs the anticausal Green's function (Fig. 12b) and shows how transmitted energy is incorporated in two-sided imaging. Note that the latter is not only valid for primaries but also multiply-scattered waves provided that all interactions between wavefield and model occur below the pseudo-source \mathbf{x}_s and pseudo-receiver \mathbf{x}_r .

Fig. 12(c) shows the causal panel of the term in eq. (12) and Fig. 12(e) shows the anticausal part of the term in eq. (13) for $EI_{PP}^1(\mathbf{x}_r, \mathbf{x}_s, t)$. Despite the complexity of the medium and the presence of perturbations both above and below the pseudo-survey line, upgoing waves are successfully reconstructed by both terms. Moreover, comparing the panels in Figs 12(c) and (e) with the true EI in Fig. 7(a) we notice how the two terms in eqs (12) and (13) are also almost transparent to downgoing waves. We can thus see that these two terms act as an approximate up/down wavefield separation filter for primaries and possibly low-order internal multiples at the EI pseudo-survey datum surface; they also do

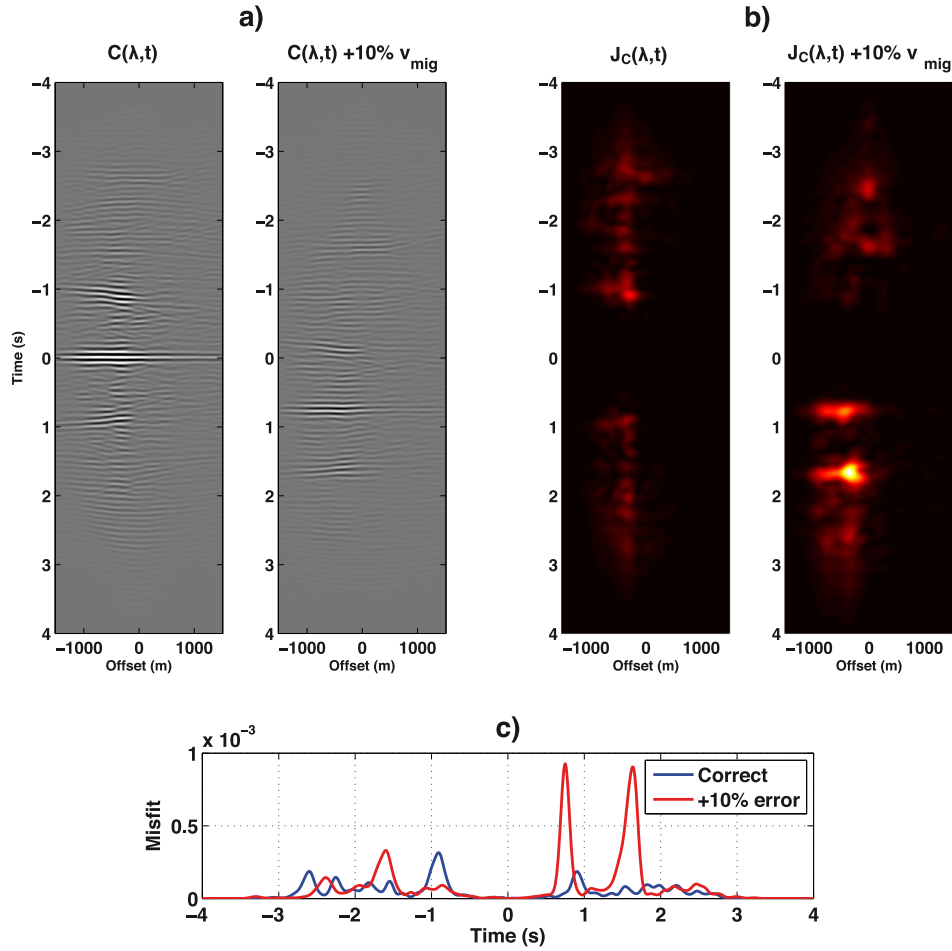


Figure 13. (a) Cross-correlation of the reflection and transmission EIs (eq. 14) and (b) penalized cross-correlation (i.e. eq. 15 before stacking over offset and time) for correct (left-hand panel) and incorrect (right-hand panel) velocity models. (c) Correlation-based objective function (eq. 15 after stacking over space but before stacking over time) for correct (blue) and incorrect (red) velocity models.

not require any local information about the medium parameters as is usually required by wavefield separation filters (e.g. Amundsen 1993).

The same two terms are then computed using the incorrect velocity models. When the EI is obtained by means of one-sided ERTM, having incorrect extrapolators results in a shift of the events in the gather to later times (Fig. 12d). Upgoing events constructed from energy in the transmitted wavefield are instead shifted in the opposite direction, and generally with different time shifts (Fig. 12f). This is explained by the fact that wave paths used to construct EI^{rf} (Fig. 12a) and EI^{tr} (Fig. 12b) are different and thus reflected and transmitted waves have different sensitivity to velocity errors. Provided that reflection data in eq. (12) and transmission data in eq. (13) are recorded, for example in situations where actual receivers are available at both the Earth's surface ($\partial V_{R,top}$) and somewhere inside the medium ($\partial V_{R,bot}$), such as in a borehole, this property can be directly exploited to design a new functional that is sensitive to migration velocity errors, or alternatively an additional regularization term for full waveform inversion (FWI) or migration velocity analysis (MVA).

We might try to quantify the time shift by temporal correlation of the two EIs, EI^{rf} and EI^{tr}

$$C(\lambda, \mathbf{x}_s, t) = EI^{rf}(\lambda, \mathbf{x}_s, t) \bar{*} EI^{tr}(\lambda, \mathbf{x}_s, -t), \quad (14)$$

where $\lambda = \mathbf{x}_s - \mathbf{x}_r$ is the offset between sources and receivers in the pseudo-gathers, and $\bar{*}$ represents correlation in the time domain. It can be observed that if the migration velocity models are correct, the cross-correlation is mainly focused around $t=0$ (Fig. 13a, left). Events at non-zero shift are also generated by ‘cross-talk’ between events in the seismogram; these events are considered to be noise in this approach, and could be further mitigated if the correlation was replaced by deconvolution.

In the presence of velocity errors, energy is shifted instead in the time axis and so is not focused at zero time (Fig. 13a, right). We conjecture that this focusing property in the EI domain can be used for velocity analysis either by minimizing the time-shift measured by picking the time of maximum energy in the correlation gather as done by Yang & Sava (2011a) for time-lag EIs, by directly penalizing such energy as done in data correlation waveform inversion (Leeuwen & Mulder 2010) or in image correlation waveform inversion (Perrone *et al.* 2015), or by dynamic warping (Hale 2014).

Following the second approach, a correlation-based objective function can be defined as

$$J_C = \frac{1}{2E_C} \|P(t)\mathcal{H}(C(\lambda, \mathbf{x}_s, t))\|_{\mathbf{x}_s, \lambda, t}^2, \quad (15)$$

where P is a penalty operator that annihilates energy at zero time and enhances energy at non-zero time lags. E_C is a normalization

factor accounting for the total energy contained in the correlation defined as $E_C = \|\mathcal{H}(C(\lambda, \mathbf{x}_s, t))\|_{\mathbf{x}_s, \lambda, t}^2$. Here we apply the Hilbert transform (\mathcal{H}) to the correlation to calculate its envelope and thus reduce phase-based fluctuations (see Fig. 13a). The penalized cross-correlations (eq. 15) are shown in Figs 13(b) and (c): the first peak at positive times in the red line carry the information about the velocity error, and it should be minimized, for example by image-domain waveform inversion.

DISCUSSION

Estimation of seismic velocities and reservoir properties in complex geologies calls for novel imaging approaches, able to provide accurate localized information at or around points in the subsurface. Scattered responses from pseudo-sources to pseudo-receivers in the subsurface, known as extended images or common-image point gathers (Vasconcelos *et al.* 2009, 2010; Yang & Sava 2011a,b; Sava & Vasconcelos 2010; Thomson 2012) represent a candidate in the image domain that could be used for these purposes. Recent studies (King *et al.* 2011; King & Curtis 2012; Meles & Curtis 2013; L  er *et al.* 2014) have shown that limited aperture arrays of sources and receivers and the knowledge of only a smoothed version of the propagation velocity model (as used in linear imaging) decrease the accuracy of these scattered wave response estimates. In particular, they showed that these acquisition limitations result in significant non-physical energy being introduced into the EIs. These studies are directly linked to the theory of source–receiver interferometry (Curtis & Halliday 2010; Halliday & Curtis 2010; Poliannikov 2011; Vasconcelos 2013; Ravasi & Curtis 2013b). SRI shows that in theory the construction of EIs requires enclosing source and receiver boundaries, and information about the location and magnitude of property perturbations in the subsurface (to construct the scattered wave propagators) in order to estimate the EI correctly. The errors that result from not satisfying these conditions are rarely negligible.

In this work, we demonstrate with a synthetic example the additional value arising from properly including internal multiples (in non-linear imaging) and transmissions (from two-sided illumination) in the construction of EIs in complex geologies. We show how discarding one or more of these contributions results in missing events, incorrect amplitudes, and spurious energy in the reconstructed pseudo-gathers. We identify two different reasons for which these contributions are beneficial: first, they construct physical events in the gather which are complementary to those constructed from primaries. For example, the reflection from the top of the salt body on the right of Fig. 4(a), which is reconstructed in the causal part of the first EI by means of linear ERTM (Fig. 7b), is reconstructed in the anticausal part of the same EI only when non-linear transmissions are accounted for in the imaging condition (Fig. 7f). Secondly, multiply-scattered waves (either reflections or transmissions) cancel some of the non-physical or spurious energy constructed by the linear imaging conditions, as shown by comparing Figs 9(e) and (f) for the P-to-S case (black arrows).

However, since the acquisition geometry used in this study (Fig. 4a) is far from the ideal situation of enclosing boundaries of sources and receivers (e.g. sources are missing below the imaging target, and sources and receivers are missing along both sides of the subsurface model), we obtain P-to-S EIs (Fig. 9) of poorer quality compared to their P-to-P counterparts (Fig. 7). The fact that violating the source and receiver equipartitioning requirement affects these two types of EIs in a different way is an indication of them having a different spatial distribution of stationary (physical

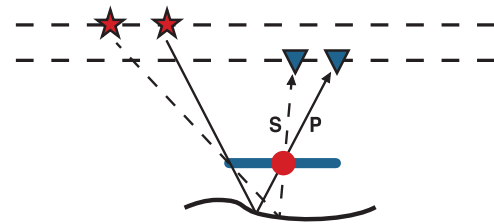


Figure 14. Two events (PP reflection and PS conversion) needed to generate PP and PS energy at a fixed pseudo-offset in the extended image.

and non-physical) contributions. As far as physical stationary points are concerned, by noting that for a fixed pseudo-offset (i.e. distance between pseudo-source and pseudo-receiver) and a given interface the converted S -wave requires an incident P -wave angle that is generally larger than that of related reflected P -wave (Fig. 14), the reconstruction of any event at large offset in the EI gather requires wider aperture acquisition (i.e. physical sources and/or receivers at farther offset) in PS imaging than in PP imaging. Furthermore, since in our example we have assumed absorbing boundaries on the sides of the subsurface model effectively creating a laterally infinite and laterally-homogenous elastic medium outside of the boundaries, P -wave sources would not suffice along the elastic portion of the enclosing source boundary and additional S -wave sources would be required to suppress all the non-physical energy generated by the available sources and receivers. On the other hand, the events that are successfully constructed in P-to-S gathers show correct amplitudes and their characteristic radiation pattern with a polarity flip around zero-offset (normal incidence). This, together with the impossibility to extract physical (meaningful) ‘true-amplitude’ P-to-S zero-offset zero-time images (Ravasi & Curtis 2013b), suggests that further research into a more suitable acquisition geometry for converted-mode EIs is necessary in future.

Although here we have assumed exact knowledge of the Earth in the models used to construct the various non-linear migration propagators, a practical way to account for multiples in these propagators also when only a reference (e.g. smoothed) version of the velocity model is available, may be to use the autofocusing techniques proposed for acoustic media by Brogini *et al.* (2012), Wapenaar *et al.* (2012) and Wapenaar *et al.* (2013), and extended to elastic media by da Costa *et al.* (2014a,b,c), Wapenaar & Slob (2014) and Wapenaar (2014). These authors have shown that it is possible to reconstruct an approximation to the correct Green’s function (i.e. the full response including internal multiples) from a virtual source anywhere inside the medium, given only the reflection data and an estimate of the direct arrival from the pseudo-source to the recording surface. This Green’s function can then be interpreted as the response observed by a pseudo-receiver in the subsurface from sources at the surface by source–receiver reciprocity. In principle, such a technique might provide the full (source- and receiver-side) propagators required by the non-linear terms in both the wavefield extrapolation and in the imaging condition in eqs (1), (2) and (3) herein.

Similarly, given standard one-sided acquisition, the autofocusing method might also be tailored to reconstruct (and then migrate) transmission data. This is specifically true if sources and receivers at the acquisition surface are co-located, and receiver arrays are also well-sampled spatially: the same source–receiver reciprocity argument as above can then be invoked to obtain the response from each source at the acquisition surface to virtual receivers at an arbitrarily selected depth level. Finally, to enable a full two-sided illumination of the imaging target (i.e. also reflection and transmission imaging from bottom sources) a further step is required: conventional

surface seismic data (i.e. sources and receivers at the surface) together with the full transmission responses obtained via autofocusing can be used to create virtual data with both sources and receivers below a selected target zone by inverting a series of multidimensional interferometric equations of convolution- and correlation-type (van der Neut *et al.* 2013).

Although unwanted non-physical events are completely suppressed in the EI when enclosing boundaries are available (or in principle, when they are constructed numerically by autofocusing), two strategies can be adopted to account for those arising from the interaction of waves propagating sideways if sources and receivers are not available (or constructed numerically) on the sides of the imaging target. These spurious events can either be prevented by appropriate spectral filtering of these fields, or mitigated directly after the EI is computed. The physical argument behind these filtering procedures is simple: any event constructed in the EI has a characteristic slope in the t - x domain, which is intrinsically related to the local dip of the reflector/discontinuity represented. Based on some assumptions about the geological structure around the pseudo-survey line of interest, we may be able limit the direction of incoming and emerging waves at the pseudo-receiver and pseudo-source locations, respectively. It is worth noting that a direct selection of the ray parameters involved in the imaging condition can also be obtained by transforming the source and receiver field in the plane-wave ($\tau - p$) domain and cross-correlating only the range of angles of interest, as recently implemented in seismic interferometry (Tao & Sen 2013).

Finally, there has been a drive towards tomographic velocity analysis (either MVA or image-domain FWI) based on EIs (Yan & Sava 2010; Fleury 2012; Fleury & Perrone 2012; Yang & Sava 2012; Shalensky *et al.* 2013). As demonstrated in our numerical example, adding non-linear terms to the imaging condition (and wavefield extrapolation) results in EIs with fewer artifacts (i.e. less coherent noise) and better focusing around zero-time, zero-offset (see close-ups in Fig. 7). We conjecture that improvements in the quality of the EIs may directly turn into a resolution improvement of these velocity analysis techniques. Moreover, since multiply-scattered waves generally travel along different paths from those of singly scattered waves, these wavepaths can also provide additional sensitivity to the model and reduce the nullspace of the tomographic operator. Two-sided illumination may also lead to new forms of migration velocity analysis when surface and borehole seismic data are jointly acquired. In fact we can compute terms that physically contribute to a certain type of events in the EI (e.g. upgoing waves) using either reflections or transmissions and then define an objective function that minimize the relative time-shift between them. We have shown that this penalty or objective function is sensitive to a 10 per cent velocity error in our complex reference model, but clearly it requires testing and analysis over a range of scenarios to assess its expected utility as a velocity analysis objective function in practice.

CONCLUSION

In this paper, we create and analyse elastic (P-to-P and P-to-S) extended images in a realistic earth model using a source-receiver interferometric (SRI) framework. We study how exploiting the energy emitted by a physical source during the seismic experiment, including primary reflections (i.e. linear imaging), multiple reflections (i.e. non-linear imaging), or transmissions (i.e. two-sided imaging), impacts the reconstruction of events in EIs.

Primary reflections from a conventional acquisition setup mainly construct upgoing and downgoing physical events in the causal and anticausal part of the EIs, respectively, but also strong non-physical waves. One type of non-physical event is due to the interaction of waves propagating sideways, and is generally characterized by a linear move-out: they can be removed via f - k filtering of the source and receiver wavefields (in pre-imaging domain), or of the EI (in post-imaging domain). In PP imaging, multiple reflections, properly included in EIs via non-linear imaging, suppress another type of non-physical arrivals (with hyperbolic-like moveout) and correct the polarities and amplitudes of some of the physical events produced by linear imaging. Transmissions construct events that are complementary to those given by reflection data (e.g. transmission data from top sources construct upgoing waves in the anticausal part and downgoing waves in the causal part), improving the time symmetry in the EIs. However, PS EIs are of poorer quality compared to their PP counterparts. Different factors that may affect the quality of PS imaging have been discussed, such as absence of S -wave sources, limited-aperture boundaries, and insufficient recording time.

EIs are also proven to be sensitive to errors in the migration velocity models: in particular it is shown that different time shifts of the same event arise in the EI when it is constructed using reflection or transmission data with incorrect velocities. This suggests that the two terms provide complementary information about velocity errors, and can be combined to design velocity analysis methods with potentially greater sensitivity to model parameters than current methods.

ACKNOWLEDGEMENTS

The authors thank the sponsors of the Edinburgh Interferometry Project (EIP) (ConocoPhillips, Schlumberger Gould Research, Statoil and Total) for supporting this research. The support offered by James Rickett (Schlumberger Gould Research) and Dirk-Jan van Manen (ETH Zurich) and their insights were essential to the development of this work. We are also grateful to the Editor Randy Keller, Joost van der Neut, and an anonymous reviewer for their invaluable comments that helped to improve the manuscript. We acknowledge the SMAART JV consortium for releasing the Pluto 1.5 synthetic dataset. This work was performed in part while Matteo Ravasi was a summer intern at Schlumberger Gould Research.

REFERENCES

- Aki, K. & Richards, P., 2002. *Quantitative Seismology*, 2nd edn, University Science Books.
- Amundsen, L., 1993. Wavenumber-based filtering of marine point source data, *Geophysics*, **58**(9), 1335–1348.
- Broggini, F., Snieder, R. & Wapenaar, K., 2012. Focusing the wavefield inside an unknown 1D medium—beyond seismic interferometry, *Geophysics*, **77**(5), A25–A28.
- Canales, L., 1984. Random noise reduction, in *Proceedings of the 54th Annual International Meeting*, SEG, Expanded Abstracts, p. 525.
- Castagna, J.P. & Backus, M.M., 1993. Offset-dependent reflectivity, in *Proceedings of the Theory and Practice of AVO Analysis*, SEG, Expanded Abstracts.
- Curtis, A., 2009. Source-receiver seismic interferometry, in *Proceedings of the 79th Annual Meeting*, SEG, Expanded Abstracts, pp. 3655–3659.
- Curtis, A. & Halliday, D., 2010. Source-receiver wave field interferometry, *Phys. Rev. E*, **81**, doi:10.1103/PhysRevE.79.056603.
- da Costa, C., Ravasi, M., Meles, G. & Curtis, A., 2014a. Elastic autofocusing, in *Proceedings of the 76th EAGE Conference & Exhibition*, Extended Abstracts.

- da Costa, C., Ravasi, M., Meles, G. & Curtis, A., 2014b. Elastic autofocusing via single-sided Marchenko inverse scattering, in *Proceedings of the 84th Annual International Meeting*, SEG, Expanded Abstracts.
- da Costa, C., Ravasi, M., Curtis, A. & Meles, G., 2014c. Elastodynamic Green's function retrieval through single-sided Marchenko inverse scattering, *Phys. Rev. E*, **90**, doi:10.1103/PhysRevE.90.063201.
- Fink, M., 2008. Time-reversal waves and super resolution, in *Journal of Physics: Conference Series*, IOP Publishing, p. 012004.
- Fleury, C., 2012. Migration velocity analysis for nonlinear reverse-time migration, in *Proceedings of the 82nd Annual International Meeting*, SEG, Expanded Abstracts.
- Fleury, C. & Perrone, F., 2012. Bi-objective optimization for the inversion of seismic reflection data: combined FWI and MVA, in *Proceedings of the 82nd Annual International Meeting*, SEG, Expanded Abstracts.
- Fleury, C. & Vasconcelos, I., 2012. Imaging condition for nonlinear scattering-based imaging: estimate of power loss in scattering, *Geophysics*, **77**(1), S1–S18.
- Foster, D.J. & Mosher, C.C., 1992. Suppression of multiple reflections using the Radon transform, *Geophysics*, **57**, 386–395.
- Gardner, G.H.F., Gardner, L.W. & Gregory, A.R., 1974. Formation velocity and density—the diagnostic basics for stratigraphic traps, *Geophysics*, **39**, 770–780.
- Hale, D., 2014. Dynamic warping of seismic images, *Geophysics*, **78**, S105–S115.
- Halliday, D. & Curtis, A., 2010. An interferometric theory of source-receiver scattering and imaging, *Geophysics*, **75**, SA95–SA103.
- Hampson, D., 1987. The discrete Radon transform: a new tool for image enhancement and noise suppression, in *Proceedings of the 57th Annual International Meeting*, SEG, Expanded Abstracts, pp. 141–143.
- Jones, I.F. & Levy, S., 1987. Signal-to-noise ratio enhancement in multichannel seismic data via the Karhunen-Loeve transform, *Geophys. Prospect.*, **3**, 12–32.
- King, S. & Curtis, A., 2012. Suppressing nonphysical reflections in Green's function estimate using source-receiver interferometry, *Geophysics*, **77**(1), Q15–Q25.
- King, S., Curtis, A. & Poole, T., 2011. Interferometric velocity analysis using physical and non-physical energy, *Geophysics*, **76**(1), SA35–SA49.
- Lerosey, G., de Rosny, J., Tourin, A. & Fink, M., 2007. Focusing beyond the diffraction limit with far-field time reversal, *Science*, **315**, 1120–1122.
- Löer, K., Meles, G.A., Curtis, A. & Vasconcelos, I., 2014. Diffracted and pseudo-physical waves from spatially-limited arrays using source-receiver interferometry (SRI), *Geophys. J. Int.*, **196**, 1043–1059.
- Mehta, K., Snieder, R., Calvert, R. & Sheiman, J., 2008. Acquisition geometry requirements for generating virtual-source data, *Leading Edge*, **27**, 620–629.
- Meles, G.A. & Curtis, A., 2013. Physical and non-physical energy in scattered wave source-receiver interferometry, *J. acoust. Soc. Am.*, **133**(6), 3790–3801.
- Meles, G.A. & Curtis, A., 2014a. Discriminating physical and non-physical diffracted energy in source-receiver interferometry, *Geophys. J. Int.*, **197**(3), 1642–1659.
- Meles, G.A. & Curtis, A., 2014b. Fingerprinting ordered diffractors in multiply diffracted waves, *Geophys. J. Int.*, **198**(3), 1701–1713.
- Ostrander, W.J., 1982. Plane-wave reflection coefficients for gas sands at nonnormal angles of incidence, in *Proceedings of the 52nd Annual International Meeting*, SEG, Expanded Abstracts, pp. 216–218.
- Perrone, F., Sava, P. & Panizzardi, J., 2015. Wavefield tomography based on local image correlations, *Geophys. Prospect.*, **63**, 35–54.
- Poliannikov, O.V., 2011. Retrieving reflections by source-receiver wavefield interferometry, *Geophysics*, **76**, SA1–SA8.
- Ravasi, M. & Curtis, A., 2013a. Elastic imaging with exact wavefield extrapolation for application to ocean bottom 4C seismic data, *Geophysics*, **78**(6), S265–S284.
- Ravasi, M. & Curtis, A., 2013b. Nonlinear scattering based imaging in elastic media: theory, theorems and imaging conditions, *Geophysics*, **78**(3), S137–S155.
- Ravasi, M., Curtis, A. & Vasconcelos, I., 2014. Beyond conventional migration: nonlinear elastic subsalt imaging with transmissions and two-sided illumination, *Geophys. J. Int.*, **198**(2), 1173–1185.
- Rutherford, S.R. & Williams, R.H., 1989. Amplitude-versus-offset variations in gas sands, *Geophysics*, **54**, 680–688.
- Sava, P. & Vasconcelos, I., 2010. Extended imaging condition for wave-equation migration, *Geophys. Prospect.*, **59**, 35–55.
- Shabelansky, A.H., Malcolm, A., Fehler, M., Shang, X. & Rodi, W., 2013. Converted phase elastic migration velocity analysis, in *Proceedings of the 83rd Annual International Meeting*, SEG, Expanded Abstracts, pp. 4732–4737.
- Simonetti, F., 2006. Multiple scattering: the key to unravel the subwavelength world from the far-field pattern of a scattered wave, *Phys. Rev. E*, **73**, doi:10.1103/PhysRevE.73.036619.
- Snieder, R., 2004. Extracting the Green's function from the correlation of coda waves: a derivation based on stationary phase, *Phys. Rev. E*, **69**, 046610.
- Snieder, R., Wapenaar, K. & Larner, K., 2006. Spurious multiples in seismic interferometry of primaries, *Geophysics*, **71**, S1111–S1124.
- Stehly, L., Campillo, M. & Shapiro, N.M., 2006. A study of the seismic noise from its long-range correlation properties, *J. geophys. Res.*, **111**, doi:10.1029/2005JB004237.
- Stoughton, D., Stefani, J. & Michell, S., 2001. 2-D elastic model for wave-field investigations of subsalt objectives, deep water Gulf of Mexico, in *Proceedings of the 71st Annual International Meeting*, SEG Expanded Abstracts, pp. 1269–1272.
- Symes, W., 2008. Migration velocity analysis and waveform inversion, *Geophys. Prospect.*, **56**, 765–790.
- Taner, M. & Koehler, F., 1969. Velocity spectra, digital computer derivation applications of velocity functions, *Geophysics*, **33**, 859–881.
- Tao, Y. & Sen, M.K., 2013. On a plane-wave based cross-correlation type seismic interferometry, *Geophysics*, **78**, Q35–Q44.
- Thomson, C., 2012. The form of the reflection operator and extended image gathers for a dipping plane reflector in two space dimensions, *Geophys. Prospect.*, **60**, 64–92.
- van Leeuwen, T. & Mulder, W.A., 2010. A correlation-based misfit criterion for wave-equation traveltome tomography, *Geophys. J. Int.*, **182**(3), 1383–1394.
- van Manen, D.-J., Robertsson, J.O.A. & Curtis, A., 2005. Modeling of wave propagation in inhomogeneous media, *Phys. Rev. Lett.*, **94**(16), doi:10.1103/PhysRevLett.94.164301
- van Manen, D.-J., Curtis, A. & Robertsson, J.O.A., 2006. Interferometric modeling of wave propagation in inhomogeneous elastic media using time reversal and reciprocity, *Geophysics*, **71**, S147–S160.
- van der Neut, J., Almagro Vidal, C., Grobde, N. & Wapenaar, K., 2013. Turning one-sided illumination into two-sided illumination by target-enclosing interferometric redatuming, in *Proceeding of the 75th EAGE Conference & Exhibition*, SEG, Expanded Abstracts.
- Vasconcelos, I., 2013. Source-receiver reverse-time imaging of dual-source, vector-acoustic seismic data, *Geophysics*, **78**(2), WA147–WA158.
- Vasconcelos, I. & Rickett, J., 2013. Broadband extended images by joint inversion of multiple blended wavefields, *Geophysics*, **78**, WA147–WA158.
- Vasconcelos, I., Sava, P. & Douma, H., 2009. Wave-equation extended images via image-domain interferometry, in *Proceeding of the 79th Annual International Meeting*, SEG, Expanded Abstracts, pp. 2839–2843.
- Vasconcelos, I., Sava, P. & Douma, H., 2010. Nonlinear extended images via image-domain interferometry, *Geophysics*, **75**, SA105–SA115.
- Vasconcelos, I., Snieder, R. & Hornby, B., 2008. Imaging internal multiples from subsalt VSP data—examples of target-oriented interferometry, *Geophysics*, **73**, S157–S168.
- Verschuur, O., 1991. Surface-related multiple elimination, an inversion approach, *PhD thesis*, Delft University of Technology.
- Wapenaar, K., 2014. Single-sided Marchenko focusing of compressional and shear waves, *Phys. Rev. E*, **90**(6), 063202.
- Wapenaar, K., Brogini, F. & Snieder, R., 2012. Creating a virtual source inside a medium from reflection data: heuristic derivation and stationary-phase analysis, *Geophys. J. Int.*, **190**(2), 1020–1024.

- Wapenaar, K., Broggini, F., Slob, E. & Snieder, R., 2013. Three-dimensional single-sided Marchenko inverse scattering, data-driven focusing, Green's function retrieval, and their mutual relations, *Phys. Rev. Lett.*, **110**(8), 084301.
- Wapenaar, K. & Fokkema, J., 2006. Green's function representations for seismic interferometry, *Geophysics*, **71**, SI33–SI46.
- Wapenaar, K. & Slob, E., 2014. On the Marchenko equation for multicomponent single-sided reflection data, *Geophys. J. Int.*, **199**, 1367–1371.
- Yan, J., 2010. Wave-mode separation for elastic imaging in transversely isotropic media, *PhD thesis*, Colorado School of Mines.
- Yan, J. & Sava, P., 2008. Isotropic angle-domain elastic reverse-time migration, *Geophysics*, **73**, S229–S239.
- Yan, J. & Sava, P., 2010. Analysis of converted-wave extended images for migration velocity analysis, in *Proceedings of the 80th Annual International Meeting*, SEG, Expanded Abstracts.
- Yang, T. & Sava, P., 2010. Moveout analysis of wave-equation extended images, *Geophysics*, **75**, 151–161.
- Yang, T. & Sava, P., 2011a. Wave-equation migration velocity analysis with time-shift imaging, *Geophys. Prospect.*, **59**, 635–650.
- Yang, T. & Sava, P., 2011b. Waveform inversion in the image, in *Proceedings of the 73rd EAGE Conference & Exhibition*, Extended Abstracts.
- Yang, T. & Sava, P., 2012. Image-domain wavefield tomography for complex geologic structures, in *Proceedings of the EAGE/ACGGP First Latin American Geophysics Workshop*.
- Yilmaz, O., 2001. *Seismic Data Analysis*, Society of Exploration Geophysics.

SUPPORTING INFORMATION

Additional Supporting Information may be found in the online version of this paper:

Figure S1. (a) *P*- and (b) *S*-wave components of the recorded data for a source at $x_S = 11$ km. Black arrows are used to indicate reflections from the two reservoirs in the recorded data.

Figure S2. P-to-P extended images obtained (a) via direct modelling and (b–h) from the four imaging experiments depicted in Fig. 5 (and from various summed combinations of their contributions) for the second survey line $EI_{PP}^2(\mathbf{x}_r, \mathbf{x}_s, t)$. Key as in Fig. 8.

Figure S3. P-to-S extended images obtained (a) via direct modelling and (b–h) from the four imaging experiments depicted in Fig. 5 (and from various summed combinations of their contributions) for the second survey line $EI_{PS}^2(\mathbf{x}_r, \mathbf{x}_s, t)$. Key as in Fig. 8.

Figure S4. P-to-P extended images obtained (a) via direct modelling and (b–h) from the four imaging experiments depicted in Fig. 5 (and from various summed combinations of their contributions) for the third (deep) survey line $EI_{PP}^3(\mathbf{x}_r, \mathbf{x}_s, t)$. Key as in Fig. 8.

Figure S5. P-to-S extended images obtained (a) via direct modelling and (b–h) from the four imaging experiments depicted in Fig. 5 (and from various summed combinations of their contributions) for the third (deep) survey line $EI_{PS}^3(\mathbf{x}_r, \mathbf{x}_s, t)$. Key as in Fig. 8.

(<http://gji.oxfordjournals.org/lookup/suppl/doi:10.1093/gji/ggv173/-/DC1>)

Please note: Oxford University Press is not responsible for the content or functionality of any supporting materials supplied by the authors. Any queries (other than missing material) should be directed to the corresponding author for the paper.